

Hybrid FEM and Peridynamic simulation of hydraulic fracture propagation in saturated porous media

Tao Ni^{a,b,c,*}, Francesco Pesavento^e, Mirco Zaccariotto^{c,d}, Ugo Galvanetto^{c,d,*}, Qi-Zhi Zhu^{a,b}, Bernhard A. Schrefler^{e,f}

^aCollege of Civil and Transportation Engineering, Hohai University, 210098, Nanjing, China

^bKey Laboratory of Ministry of Education for Geomechanics and Embankment Engineering, Hohai University, Nanjing, China

^cIndustrial Engineering Department, University of Padova, via Venezia 1, Padova, 35131, Italy

^dCenter of Studies and Activities for Space (CISAS)-G. Colombo, via Venezia 15, Padova, 35131, Italy

^eDepartment of Civil, Environmental and Architectural Engineering, University of Padova, via Marzolo 9, Padova, 35131, Italy

^fInstitute for Advanced Study, Technische Universität München, Lichtenbergstrasse 2a, D-85748 Garching b. München, Germany

Abstract

This paper presents a hybrid modelling approach for simulating hydraulic fracture propagation in saturated porous media: ordinary state-based peridynamics is used to describe the behavior of the solid phase, including the deformation and crack propagation, while FEM is used to describe the fluid flow and to evaluate the pore pressure. Classical Biot poroelasticity theory is adopted. The proposed approach is first verified by comparing its results with the exact solutions of two examples. Subsequently, a series of pressure- and fluid-driven crack propagation examples are solved and presented. The phenomenon of fluid pressure oscillation is observed in the fluid-driven crack propagation examples, which is consistent with previous experimental and numerical evidences. All the presented examples demonstrate the capability of the proposed approach in solving problems of hydraulic fracture propagation in saturated porous media.

Keywords: Peridynamics, Hydraulic fracture propagation, Saturated porous media, Finite element method

1. Introduction

Hydraulic fracture (HF) is an effective technology to improve the recovery rate of natural resources (oil, gas etc.) from reservoirs with low-permeability [1]. The cracks produced by hydraulic fracturing connect the resources in the reservoirs with the wellbores, which allows to extract a vast amount of resources inaccessible in the past and provides great economic benefits [2]. However, cracks may also lead to leakage of the natural resources and to groundwater contamination [3, 4]. Furthermore, the

*Corresponding author

Email addresses: hhunitao@hhu.edu.cn (Tao Ni), ugo.galvanetto@unipd.it (Ugo Galvanetto)

hydraulic fracturing mining process may also result in air and surface pollution around the mining area [5]. Therefore, accurate prediction of hydraulic fracture consequences in unconventional hydrocarbon reservoirs has a great relevance in guiding the exploitation of natural resources [6, 7, 8], as well as in balancing the vast economic benefits with the environmental risks.

The numerical study of the HF propagation in deformable porous media has become a major research topic in mechanical, energy and environmental engineering during the past decades [2, 5, 9]. HF is a typical hydro-mechanical coupled problem involving deformation and fracture evolution of the solid phase as well as fluid flow in the fractured area. To solve this type of coupled system, a variety of complex numerical models have been developed [10], which can be simply classified into three categories: continuous, discrete and hybrid approaches. The typical continuous approaches mainly refer to the computational techniques based on the finite element method. These approaches are potentially appropriate for irregular body shapes with heterogeneous material properties and non-linear behavior. In [11, 12, 13], the adaptive re-meshing technique is used to follow the crack surfaces during the hydraulic fracturing process. Re-meshing is usually computationally expensive and it is difficult to develop robust schemes considering mass and momenta conservation [13]. Cohesive zone models with interface elements are developed for the HF cases of known fracture paths [14, 15, 16, 17, 18]. A fine mesh is required to accurately simulate both the toughness and viscosity of the HF propagation. The simulation results are seriously affected by the details of the cohesive constitutive law in the cases with a large cohesive zone [14, 18, 19]. Cohesive zone models can also be used in more general cases with unknown crack paths by either inserting cohesive interface elements between all finite elements of the mesh or inserting them adaptively between the yielding finite elements [10, 11]. By performing the enrichment locally in the elements intersected by a discontinuity, the extended finite element method (XFEM) has the ability to simulate the crack propagation [20], which can be used to solve HF problems [21, 22, 23, 24]. Combined with the cohesive zone models, XFEM can produce the solutions of plane-strain HF propagation cases [16, 25] and is widely used to analyse static or dynamic HF problems [26, 27, 28, 29]. Nevertheless, the XFEM-based approaches are still facing the challenges of dealing with multi-cracks and 3D non-planar crack problems [30, 31]. Another continuous method for HF problems is the phase field method (PFM), in which a continuous scalar variable called the *field order parameter* or *crack field* is introduced to describe a smooth transition between the intact and the fully broken regions [32]. The PFM is usually solved in the FE framework and in the discretization the crack is located by smearing it over few elements [33]. The extension of the PFM to poroelastic media is available in [9, 34, 35, 36]. But while the smeared nature of the PFM allows it to model complex fracture behavior, it also limits its capability to accurately represent the displacement discontinuities across the crack surface. Other continuous approaches for simulating

HF problems are those based on the boundary element method [37, 38, 39, 40, 41] and on meshless techniques [42, 43].

The discrete approaches for HF are usually based on the discrete element method (DEM), including the particle models [44, 45] and the lattice models [44, 46]. In the DEM, the particles with different sizes and shapes are assembled to represent the solid medium, the deformation is described through the displacement of the particles while the internal forces are expressed by the contacts between the particles. The loss of contact indicates the formation of cracks. By introducing the expression of fluid flow through the transport elements or finite volume scheme, the DEM is applied to simulate the hydraulic fracturing behavior [44, 45, 46].

In order to combine the advantages of different approaches, some hybrid approaches have been proposed, for example, the combined finite-discrete element method in [47, 48], the hybrid discrete-fracture/matrix and multi-continuum model in [49] and a hybrid discrete-continuum method in [50]. In addition, other attempts have been implemented, such as the numerical manifold method [51, 52], the discretized virtual internal bond method [53] and the distinct lattice spring model [54, 55]. Although a large number of numerical approaches have been proposed for HF problems, they still have some shortcomings and are facing challenges in dealing with the problems of multi-cracks, crack bifurcation or leak-off particularly for 3D conditions.

The theory of peridynamics (PD) was firstly introduced by Silling in 2000 [56]. It is a non-local continuum theory based on integro-differential equations. It is particularly suited to simulate crack propagation in structures since it allows cracks to grow naturally without resorting to external crack growth criteria. The first version of the PD theory, called Bond-Based PD (BB-PD), had a strong limitation because the Poisson's ratio could only assume a fixed value [57, 58, 59, 60, 61]. The present paper makes use of the Ordinary State-Based PD theory (OSB-PD) [62]. However, some other modified versions of the theory were also developed for solid materials with any Poisson's ratio [63, 64, 65, 66, 67, 68]. The application of the PD models to HF problems can be traced back to [6], in which the problems of consolidation and leak-off in HF are solved with an extended SB-PD model. The hydro-mechanical coupling in [6] is introduced according to Biot theory with a given pore pressure field, without considering the fluid flow in the porous media. Subsequently, the PD theory for single-phase fluid flow in porous media was developed in [69, 70], in which non-local fluid transport in domains with discontinuities is considered in the context of peridynamics. Based on the proposed PD porous flow model and the extended SB-PD model, a fully coupled PD model for HF problems was presented in [7]. In the fully coupled model, it assumes that a fracture space is created in any two adjacent material points when they separate beyond the critical stretch and the damage values for both the points reach a preset value. Such material points are referred as "dual points", not only

acting as porous material but also representing the fracture space for fluid to flow in between them. The permeability at “dual points” is computed by using the cubic law, where the fracture width used in the cubic law is defined according to the numerically evaluated reservoir porosity. Later, the fully coupled PD model is applied to the analysis of several typical HF cases in [8, 71]. Several other works on the application of PD in hydro-mechanical coupled problems can be found in [72, 73, 74]. In [72], a state-based viscoelastic peridynamic approach is developed and applied in the simulation of the fracturing process under hydraulic loading without mentioning how to compute the fluid flow field. In [73], a fully coupled poroelastic formulation is presented in the context of bond-based PD theory and applied to fluid-filled fractures, and the non-local governing equation of fluid flow is also given, but the fluid flowing in cracks seems not be considered. The implicit implementation of the fully coupled PD model from [7] is made in [74] and used for solving consolidation problem and dynamic analysis of saturated porous media without considering crack propagation. In addition to above work, a numerical framework of coupling peridynamics with a edge-based finite element model for simulating HF process in Karoo is introduced in brief in [75]. However, no detailed implementation is mentioned, and so far, no subsequent work has been published.

PD-based numerical approaches are usually more computationally expensive than those making use of local mechanics and FEM [58, 76]. For that reason and inspired by [54], in this paper, a hybrid modelling approach making use of FEM and PD is proposed for simulating the hydraulic fracturing in saturated porous media. PD is used to describe the deformation of the solid skeleton and to capture the advancement of cracks, while FEM equations are used to describe the fluid mechanics. The hydro-mechanical coupling is based on Biot theory. In the FEM equations, the coupling terms are considered as local expression, whereas in PD equations, the pore pressures are applied non-locally. A staggered scheme is adopted to solve the coupled system. In each solution sequence, the pressure field is solved first by using an implicit time integration scheme from [77, 78], and then the adaptive dynamic relaxation method [79, 80, 81] is used to compute the displacement field. The solution algorithms for solving the transient analysis of consolidation and fluid flow are also presented. The relevant software is developed in MATLAB. With the developed software, a series of numerical examples are performed to validate the proposed approach and to demonstrate its main features. The main contributions of the paper are:

- The FEM and peridynamic models are combined to solve the hydro-mechanical coupled problems;
- The coupling is described in detail and the coupling matrix of a PD bond is presented;
- An algorithm for computing the aperture of the cracks is presented, which is much simpler than

the normal displacement jump approach used in [9];

- The proposed approach is applied successfully in the simulation of HF propagation and bifurcation. In the fluid-driven cases, the pressure oscillation phenomenon discussed in [29] is observed, which indicates the capability of the proposed method to describe the dynamic behaviors in HF problems.

The contents of this paper are organized as follows. In *sect. 2*, the OSB-PD theory is first briefly summarized and extended for poroelastic media by using the effective stress principle, then the governing equations for the fluid flow in fractured porous media are introduced. *Sect. 3* presents the numerical implementation in detail. In *sect. 4*, the accuracy of the numerical simulation is verified by using two examples, then a series of pressure- and fluid-driven HF cases are presented for further describing the performance of the hybrid approach. Finally, *sect. 5* concludes the paper.

2. Theoretical basis

2.1. The extended ordinary state-based peridynamic model for saturated porous media

2.1.1. Basic concepts

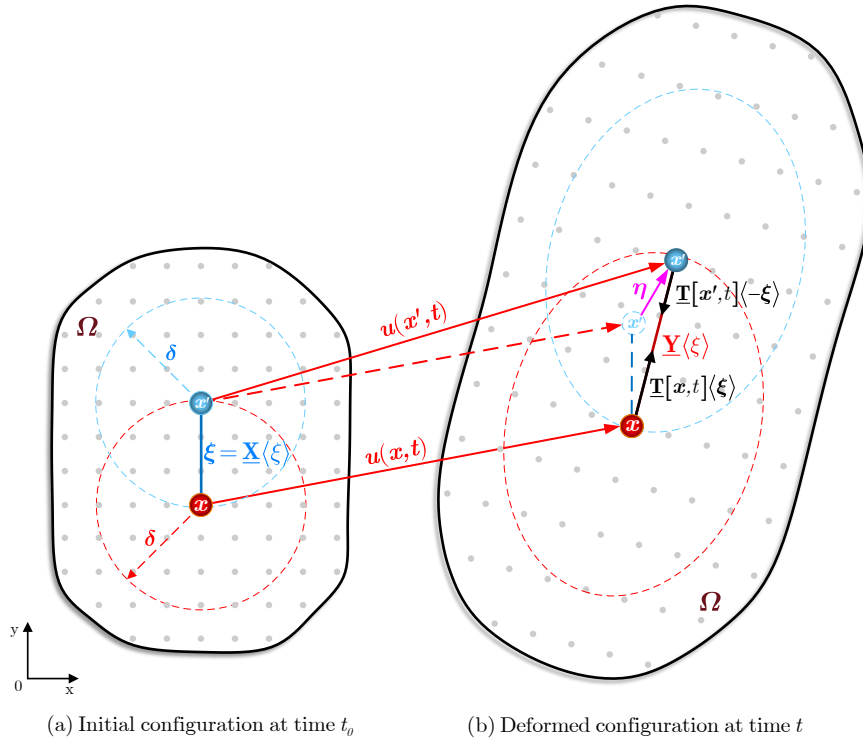


Figure 1: The positions of two material points in the (a) initial and (b) deformed configurations.

As shown in Fig. 1, a domain Ω is modelled by OSB-PD, in which each point interacts with all the other points around it within a prescribed horizon radius δ [62, 82, 83, 84, 85, 86]. Let us consider

two points \mathbf{x} and \mathbf{x}' in the initial configuration of domain Ω (see Fig. 1a). The bond connecting these two points, that represents their relative position, can be expressed as:

$$\boldsymbol{\xi} = \mathbf{x}' - \mathbf{x} \quad (1)$$

If \mathbf{u} and \mathbf{u}' are the displacements of \mathbf{x} and \mathbf{x}' respectively, then the relative displacement vector can be given by:

$$\boldsymbol{\eta} = \mathbf{u}' - \mathbf{u} \quad (2)$$

The reference position vector state and deformation vector state are defined as $\underline{\mathbf{X}} \langle \boldsymbol{\xi} \rangle$ and $\underline{\mathbf{Y}} \langle \boldsymbol{\xi} \rangle$, respectively, and are given by the following expressions:

$$\underline{\mathbf{X}} \langle \boldsymbol{\xi} \rangle = \boldsymbol{\xi} \quad , \quad \underline{\mathbf{Y}} \langle \boldsymbol{\xi} \rangle = \boldsymbol{\xi} + \boldsymbol{\eta} \quad (3)$$

The reference position scalar state and deformation scalar state are defined as:

$$\underline{x} = \|\underline{\mathbf{X}}\| \quad , \quad \underline{y} = \|\underline{\mathbf{Y}}\| \quad (4)$$

where $\|\underline{\mathbf{X}}\|$ and $\|\underline{\mathbf{Y}}\|$ are the norms of $\underline{\mathbf{X}}$ and $\underline{\mathbf{Y}}$, representing the lengths of the bond in its initial and deformed states, respectively. For later use, a unit state in the direction of $\underline{\mathbf{Y}}$ is defined as:

$$\underline{\mathbf{M}} \langle \boldsymbol{\xi} \rangle = \frac{\underline{\mathbf{Y}}}{\|\underline{\mathbf{Y}}\|} \quad (5)$$

In addition, the extension scalar state is defined to describe the longitudinal deformation of the bond:

$$\underline{e} = \underline{y} - \underline{x} \quad (6)$$

In the deformed configuration, shown in Fig. 1b, the force density vector states at time t are defined as $\underline{\mathbf{T}}[\mathbf{x}, t] \langle \boldsymbol{\xi} \rangle$ and $\underline{\mathbf{T}}[\mathbf{x}', t] \langle -\boldsymbol{\xi} \rangle$ along the deformed bond, and their values can be different. Thus, the OSB-PD equation of motion is given as [85]:

$$\rho \ddot{\mathbf{u}}(\mathbf{x}, t) = \int_{\mathcal{H}_x} \{ \underline{\mathbf{T}}[\mathbf{x}, t] \langle \boldsymbol{\xi} \rangle - \underline{\mathbf{T}}[\mathbf{x}', t] \langle -\boldsymbol{\xi} \rangle \} dV_{x'} + \mathbf{b}(\mathbf{x}, t) \quad (7)$$

where $dV_{x'}$ is the infinitesimal volume associated to point \mathbf{x}' . \mathbf{b} is the force density of the external body force. \mathcal{H}_x is the neighborhood associated with the material point \mathbf{x} , which is usually a circle in

2D and a sphere in 3D, it is mathematically defined as: $\mathcal{H}_x(\delta) = \{x \in \Omega: \|\boldsymbol{\xi}\| \leq \delta\}$.

2.1.2. Linear isotropic solid material

According to [62, 84, 85], the 3D elastic strain energy density at point \boldsymbol{x} in a linear OSB-PD isotropic material can be expressed as:

$$W(\theta, \underline{e}^d) = \frac{\kappa\theta^2}{2} + \frac{15\mu}{2m} \int_{\mathcal{H}_x} \underline{w} \underline{e}^d \underline{e}^d dV_{x'} \quad (8)$$

where k and μ are bulk modulus and shear modulus. θ is the volume dilatation value, \underline{e}^d is the deviatoric extension state, and they are defined as:

$$\theta = \frac{3}{m} \int_{\mathcal{H}_x} (\underline{w} \underline{x} \underline{e}) dV_{x'} \quad (9)$$

$$\underline{e}^d = \underline{e} - \frac{\theta \underline{x}}{3} \quad (10)$$

in which m is called the weighted volume, given as:

$$m = \int_{\mathcal{H}_x} \underline{w} \|\boldsymbol{\xi}\|^2 dV_{x'} \quad (11)$$

In the above formulae, \underline{w} is an influence function, which is usually adopted as $\underline{w} = \exp\left(-\frac{\|\boldsymbol{\xi}\|^2}{\delta^2}\right)$. Based on the above notions, the force density vector state \mathbf{T} can be defined as:

$$\mathbf{T} = \underline{t} \cdot \underline{\mathbf{M}} \quad (12)$$

where \underline{t} is called the force density scalar state. In [85], \underline{t} is defined in 3D context as:

$$\underline{t} = 3\kappa\theta \frac{\underline{w} \underline{x}}{m} + 15\mu \underline{e}^d \frac{\underline{w}}{m} \quad (13)$$

The expression of PD force density scalar state in plane strain conditions is also introduced [81]:

$$\underline{t} = 2\left(\kappa - \frac{\mu}{3}\right)\theta \frac{\underline{w} \underline{x}}{m} + 8\mu \underline{e}^d \frac{\underline{w}}{m} \quad (14)$$

where θ is calculated by:

$$\theta = \frac{2}{m} \int_{\mathcal{H}_x} (\underline{w} \underline{x} \underline{e}) dV_{x'} \quad (15)$$

2.1.3. Failure criterion

To describe the material failure and crack propagation, a failure criterion is required in the PD-based numerical models. Three different types of failure criteria are commonly used in SB-PD models. The first is called “critical bond stretch” criterion [57]. It was derived in the context of the BB-PD theory based on mode I fracture. The second is the bond-level energy based failure criterion derived as in the critical bond stretch criterion but involving deviatoric deformation [87]. The bond-level energy based criterion is thoroughly introduced and successfully applied to the quantitative fracture analysis of isotropic and orthotropic materials in [88, 89]. The last criterion is an alternative bond failure criterion in terms of strain invariants introduced in [90], which can be used as a bridge to directly apply the damage model of the classical theory of mechanics in peridynamics. As discussed in [91], all the three criteria can be suitable in the analysis of mode I fracture problems and reproduce the experimentally observed behavior. In the considered HF problems, the fracture mainly occurs with the opening crack propagation, hence for simplicity and following the recommendation in [92], the “critical bond stretch” criterion is adopted for the SB-PD model in this paper.

The stretch value of bond ξ is defined as [81]:

$$s \langle \xi \rangle = \frac{\underline{e} \langle \xi \rangle}{\underline{x} \langle \xi \rangle} \quad (16)$$

and the critical stretch value can be expressed as [76, 93, 94]:

$$s_c = \begin{cases} \sqrt{\frac{5G_c}{6E\delta}} & , \quad 3D \\ \sqrt{\frac{5G_c}{12E\delta}} & , \quad \text{plane strain} \end{cases} \quad (17)$$

where G_c is the critical energy release rate for mode I fracture. Eq. (17) was described in [76, 93] for the case of BB-PD. Its use in SB-PD is not fully justified, but it is usually accepted [91, 92].

In addition, a scalar variable ϱ is introduced in the OSB-PD models to indicate the connection status of the bonds [76, 93]:

$$\underline{\varrho} \langle \xi \rangle = \begin{cases} 1 & , \quad \text{if } s \langle \xi \rangle < s_c , \text{ for all } 0 < \bar{t} < t \\ 0 & , \quad \text{otherwise} \end{cases} \quad (18)$$

thus the damage value φ_x at point \mathbf{x} in the system can be defined as:

$$\varphi_x = 1 - \frac{\int_{\mathcal{H}_x} \underline{w} \langle \xi \rangle \underline{\varrho} \langle \xi \rangle dV_{x'}}{\int_{\mathcal{H}_x} \underline{w} \langle \xi \rangle dV_{x'}} \quad (19)$$

Let us consider a material point \boldsymbol{x} existing in a cracked solid modeled by peridynamics, as shown

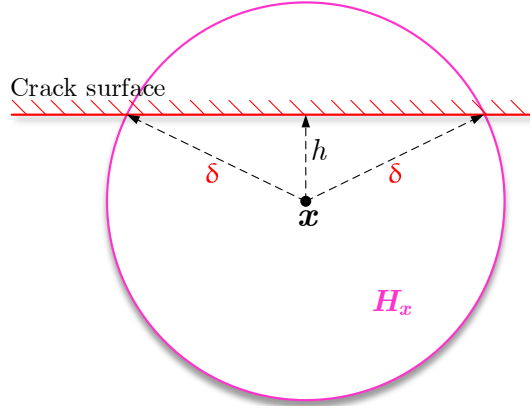


Figure 2: Neighborhood of point \boldsymbol{x} crossed by a crack.

in Fig. 2, the neighborhood of point \boldsymbol{x} is crossed by a crack. The area on the upper side of the crack can be given as:

$$S_{up} = \frac{1}{2} \arccos \left(\left(\frac{h}{\delta} \right)^2 - 1 \right) \delta^2 - h \sqrt{\delta^2 - h^2} \quad (20)$$

The damage value φ_x at the point \boldsymbol{x} can be represented geometrically with the ratio of the S_{up} to the total area of the neighborhood, which is given as:

$$\varphi_x = \frac{1}{2\pi} \left[\arccos \left(2 \left(\frac{h}{\delta} \right)^2 - 1 \right) - 2 \frac{h}{\delta} \sqrt{1 - \left(\frac{h}{\delta} \right)^2} \right] \quad (21)$$

The evolution of damage value φ_x as the position changes is expressed in Fig. 3. Thus, the value of φ_x theoretically ranges from 0 to 0.5 at the continuous level.

2.1.4. Effective stress principle in ordinary state-based peridynamics

In the theory of single-phase fluid saturated porous media [95, 96], the effective stress principle is expressed as:

$$\boldsymbol{\sigma}^{tot} = \boldsymbol{\sigma}^{eff} - \alpha \boldsymbol{I} p \quad (22)$$

where $\boldsymbol{\sigma}^{tot}$ and $\boldsymbol{\sigma}^{eff}$ are the total and the effective stress tensors, α is the Biot coefficient, p is the pore pressure, and \boldsymbol{I} is the unit tensor. In Eq.(22), the negative sign is introduced as it is a general convention to take tensile components of stress as positive [96].

In Eq.(13), the force density scalar state has been divided into a dilatational term, $3\kappa\theta\frac{w}{m}\boldsymbol{x}$, and a deviatoric term, $15\mu\boldsymbol{e}^d\frac{w}{m}$. In classical continuum theory, the volume dilatation is defined by $\theta =$

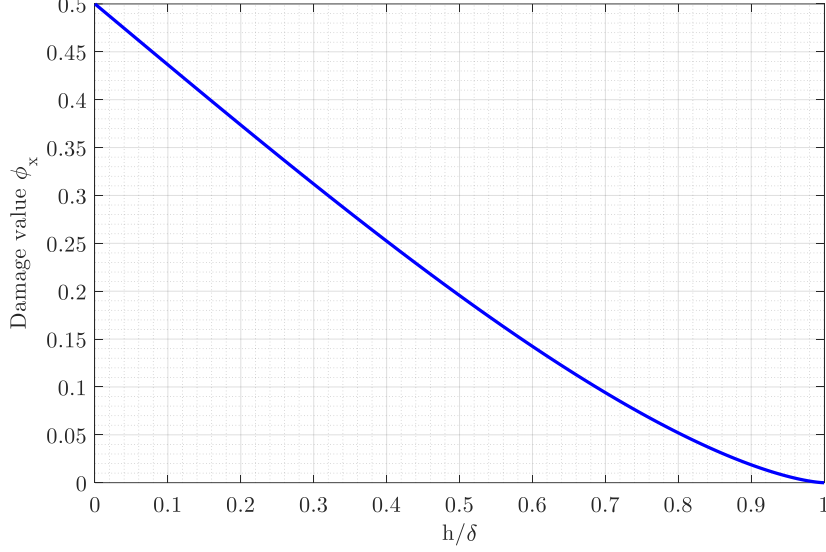


Figure 3: Evolution of damage value φ_x as the position changes.

$\varepsilon_{xx} + \varepsilon_{yy} + \varepsilon_{zz}$. By neglecting the coefficient part related to the discretization, the dilatational term in the force density scalar state should correspond to volume stress, $(\sigma_{xx} + \sigma_{yy} + \sigma_{zz})/3$, in classical continuum solid theory. Thus, by using the effective stress principle expressed in Eq.(22), the pore pressure term can be directly added to the dilatational term and the expression of the force density scalar state for the 3D problem of saturated porous media can be obtained as [6, 74, 97]:

$$\begin{aligned} \underline{t}^{tot} &= 3(\kappa\theta - \alpha p) \frac{w}{m} \underline{x} + 15\mu e^d \frac{w}{m} \\ &\Downarrow \\ \underline{t}^{tot} &= \underline{t}^{eff} - 3\alpha p \frac{w}{m} \underline{x} \end{aligned} \quad (23)$$

in which, \underline{t}^{eff} corresponds to \underline{t} in Eq. (13).

Thus, the coupled peridynamic equation of motion will be given as:

$$\begin{aligned} \rho \ddot{\mathbf{u}}(\mathbf{x}, t) &= \int_{\mathcal{H}_x} \{ \underline{\mathbf{T}}[\mathbf{x}, p, t] \langle \underline{\boldsymbol{\xi}} \rangle - \underline{\mathbf{T}}[\mathbf{x}', p', t] \langle -\underline{\boldsymbol{\xi}} \rangle \} dV_{x'} + \mathbf{b}(\mathbf{x}, t) \\ &= \int_{\mathcal{H}_x} \{ \underline{\mathbf{T}}[\mathbf{x}, t] \langle \underline{\boldsymbol{\xi}} \rangle - \underline{\mathbf{T}}[\mathbf{x}', t] \langle -\underline{\boldsymbol{\xi}} \rangle \} dV_{x'} - 3\alpha \int_{\mathcal{H}_x} \left[p \frac{w}{m(\mathbf{x})} \underline{\mathbf{M}} \langle \underline{\boldsymbol{\xi}} \rangle - p' \frac{w}{m(\mathbf{x}')} \underline{\mathbf{M}} \langle -\underline{\boldsymbol{\xi}} \rangle \right] dV_{x'} + \mathbf{b}(\mathbf{x}, t) \end{aligned} \quad (24)$$

where p and p' are the values of pore pressure at nodes \mathbf{x} and \mathbf{x}' .

In addition, the expression of the force density scalar state for the 2D problem will be obtained similarly:

$$\underline{t}^{tot} = \underline{t}^{eff} - 2\alpha p \frac{w}{m} \underline{x} \quad (25)$$

in which \underline{t}^{eff} is the force density scalar state in plane strain cases expressed in Eq. (14).

2.2. Governing equations for flow in fractured porous media

To formulate the governing equation for flow in the domain Ω , the whole domain Ω is divided into three parts: Ω_r , Ω_f and Ω_t (see Fig. 4a), representing the unbroken domain (reservoir domain), the fracture domain and the transition domain between Ω_r and Ω_f . Following references [1, 2, 9], we use the peridynamic damage field (φ in Eq. (19)) as an indicator. As shown in Fig. 4b, two threshold values (c_1 and c_2) are set to identify the three flow domains: the reservoir domain is defined as $\varphi \leq c_1$, the fracture domain as $\varphi \geq c_2$ and the transition domain as $c_1 \leq \varphi \leq c_2$.

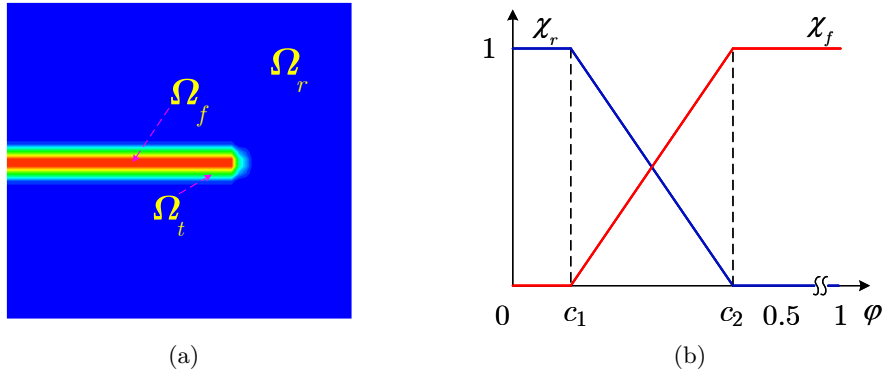


Figure 4: (a) The definition of the Ω_r , Ω_t and Ω_f ; (b) linear indicator functions χ_r and χ_f .

We use Darcy's law to describe the flow field in the saturated porous media, then the mass balance in the reservoir domain is given as:

$$\rho_r s_r \frac{\partial p}{\partial t} + \rho_r \alpha_r \frac{\partial \varepsilon_v}{\partial t} + \rho_r \nabla \cdot \left[\frac{k_r}{\mu_w} (-\nabla p + \rho_r g) \right] = q_r \quad (26)$$

where α_r , s_r , k_r , q_r and ρ_r are the Biot coefficient, storage coefficient, permeability, source term and the density of the media in the reservoir domain, respectively; μ_w is the viscosity coefficient of the fluid in the reservoir domain. g is gravity and ε_v is volumetric strain. The storage coefficient is given as:

$$s_r = \frac{(\alpha_r - n_r)(1 - \alpha_r)}{K_r} + \frac{n_r}{K_w} \quad (27)$$

where K_r and K_w are the bulk moduli of solid and fluid in the reservoir domain, n_r is the porosity.

In order to use cubic law to evaluate the permeability in the fracture domain, the fracture domain needs to be assumed fully filled by fluid and the porosity $n_f = 1$ is adopted. Supposing that the fluid

in the fracture is incompressible, the volumetric strain term in Eq. (26) vanishes [9, 98]:

$$\rho_f s_f \frac{\partial p}{\partial t} + \rho_f \nabla \cdot \left[\frac{k_f}{\mu_w} (-\nabla p + \rho_f g) \right] = q_f \quad (28)$$

where s_f , k_f , q_f and ρ_f are the storage coefficient, permeability, source term and the density of the fluid in the fracture domain.

Following the descriptions in [1, 2, 9], two linear indicator functions are defined to connect the transition domain with the reservoir and fracture domains: χ_r and χ_f , which satisfy:

$$\chi_r(\cdot, \varphi) := \chi_r(\mathbf{x}, t, \varphi) = 1 \text{ in } \Omega_r(t) \text{ and } \chi_r(\cdot, \varphi) = 0 \text{ in } \Omega_f(t) \quad (29)$$

$$\chi_f(\cdot, \varphi) := \chi_f(\mathbf{x}, t, \varphi) = 1 \text{ in } \Omega_f(t) \text{ and } \chi_f(\cdot, \varphi) = 0 \text{ in } \Omega_r(t) \quad (30)$$

In the transition domain, the two linear functions are defined as (see Fig. 4b):

$$\chi_r(\cdot, \varphi) = \frac{c_2 - \varphi}{c_2 - c_1}, \text{ and } \chi_f(\cdot, \varphi) = \frac{\varphi - c_1}{c_2 - c_1} \quad (31)$$

The detailed illustration of the linear indicator functions χ_r and χ_f can be found in [1, 2, 9]. Fluid and solid properties in the transition domain can be obtained by interpolating those properties of reservoir and fracture domains by using the indicator functions: $\rho_T = \rho_r \chi_r + \rho_f \chi_f$, $\alpha_T = \alpha_r \chi_r + \alpha_f \chi_f$, $n_T = n_r \chi_r + n_f \chi_f$, $k_T = k_r \chi_r + k_f \chi_f$, $s_T = s_r \chi_r + s_f \chi_f$. **It should be noted in particular that the Biot coefficient in the fracture domain is taken as $\alpha_f = 1$.** Therefore, the governing equation for the flow in the transition domain can be given as:

$$\rho_T s_T \frac{\partial p}{\partial t} + \rho_T \alpha_T \frac{\partial \varepsilon_v}{\partial t} + \rho_T \nabla \cdot \left[\frac{k_T}{\mu_w} (-\nabla p + \rho_T g) \right] = q_T \quad (32)$$

Moreover, the cubic law is used to evaluate the permeability of the fracture domain [55, 99]:

$$k_f = \frac{1}{12} a^2 \quad (33)$$

where a is the aperture of the crack, which can be obtained by using the method described in *sect.* 3.3.

3. Discretization and numerical implementation

3.1. FEM discretization of the governing equation for the fluid flow

Using the Galerkin finite element method, the discretized governing equations of the fluid flow in classical continuum theory assume the following form [95]:

$$\mathbf{S}\dot{\mathbf{p}} + \mathbf{Q}^T \dot{\mathbf{u}} + \mathbf{H}\mathbf{p} = \mathbf{q}^w \quad (34)$$

where: \mathbf{Q} is the coupling matrix, \mathbf{H} is the permeability matrix, \mathbf{S} is the compressibility matrix, all of them can be obtained by assembling the corresponding element matrices. When using the shape functions N_u (for displacement) and N_p (for pressure), the matrices in Eq.(34) can be given as [54, 100]:

$$\mathbf{Q} = \int_{\Omega} (\mathbf{L}N_u)^T \alpha \mathbf{m} N_p d\Omega \quad (35)$$

$$\mathbf{H} = \int_{\Omega} (\nabla N_p)^T \frac{k}{\mu_w} (\nabla N_p) d\Omega \quad (36)$$

$$\mathbf{S} = \int_{\Omega} N_p^T s N_p d\Omega \quad (37)$$

in which \mathbf{L} is the differential operator defined as:

$$\mathbf{L} = \begin{bmatrix} \frac{\partial}{\partial x} & 0 & 0 \\ 0 & \frac{\partial}{\partial y} & 0 \\ 0 & 0 & \frac{\partial}{\partial z} \\ \frac{\partial}{\partial y} & \frac{\partial}{\partial x} & 0 \\ 0 & \frac{\partial}{\partial z} & \frac{\partial}{\partial y} \\ \frac{\partial}{\partial z} & 0 & \frac{\partial}{\partial x} \end{bmatrix} \quad (38)$$

\mathbf{m} is a vector used instead of the unit tensor \mathbf{I} in Eq.(22) given as:

$$\mathbf{m} = [1, 1, 1, 0, 0, 0]^T \quad (39)$$

Note that the coupling term $(\rho\alpha \frac{\partial \varepsilon_v}{\partial t})$ caused by volumetric change will be removed from the governing equation for the flow in the fracture domain.

3.2. Discretization of the peridynamic equations

After discretization, the peridynamic equation of motion of the current node \mathbf{x}_i is written as:

$$\begin{aligned} \rho \ddot{\mathbf{u}}_i^t = & \sum_{j=1}^{N_{H_i}} \{ \mathbf{T}[\mathbf{x}_i, t] \langle \boldsymbol{\xi}_{ij} \rangle - \mathbf{T}[\mathbf{x}_j, t] \langle -\boldsymbol{\xi}_{ij} \rangle \} \cdot V_j \\ & - 3\alpha \sum_{j=1}^{N_{H_i}} \left[p_i \frac{w \langle \boldsymbol{\xi}_{ij} \rangle \underline{x} \langle \boldsymbol{\xi}_{ij} \rangle}{m(\mathbf{x}_i)} \underline{\mathbf{M}} \langle \boldsymbol{\xi}_{ij} \rangle - p_j \frac{w \langle \boldsymbol{\xi}_{ij} \rangle \underline{x} \langle \boldsymbol{\xi}_{ij} \rangle}{m(\mathbf{x}_j)} \underline{\mathbf{M}} \langle -\boldsymbol{\xi}_{ij} \rangle \right] \cdot V_j + \mathbf{b}_i^t \end{aligned} \quad (40)$$

where N_{H_i} is the number of family nodes of \mathbf{x}_i , \mathbf{x}_j is \mathbf{x}_i 's family node, V_j is the volume of node \mathbf{x}_j .

Under the assumption of small deformation, the global form of Eq.(40) can be written as:

$$\mathbf{M}^{PD} \ddot{\mathbf{u}} + \mathbf{K}^{PD} \mathbf{u} - \mathbf{Q}^{PD} p = f^{PD} \quad (41)$$

in which \mathbf{M}^{PD} , \mathbf{K}^{PD} and \mathbf{Q}^{PD} are the mass, stiffness and ‘‘coupling’’ matrices of the PD domain, respectively. Note that \mathbf{M}^{PD} is usually taken as lumped mass matrix. The method of obtaining \mathbf{K}^{PD} of OSB-PD equations can be found in [83]. Assume that $\underline{\mathbf{M}} \langle \boldsymbol{\xi}_{ij} \rangle = [M_x, M_y, M_z]$, then the ‘‘coupling’’ matrix for $\boldsymbol{\xi}_{ij}$ can be given as:

$$\mathbf{Q}_{ij}^{PD} = 3\alpha \underline{w} \langle \boldsymbol{\xi}_{ij} \rangle \underline{x} \langle \boldsymbol{\xi}_{ij} \rangle V_i V_j \begin{bmatrix} \frac{M_x}{m(\mathbf{x}_i)} & \frac{M_x}{m(\mathbf{x}_j)} \\ \frac{M_y}{m(\mathbf{x}_i)} & \frac{M_y}{m(\mathbf{x}_j)} \\ \frac{M_z}{m(\mathbf{x}_i)} & \frac{M_z}{m(\mathbf{x}_j)} \\ -\frac{M_x}{m(\mathbf{x}_i)} & -\frac{M_x}{m(\mathbf{x}_j)} \\ -\frac{M_y}{m(\mathbf{x}_i)} & -\frac{M_y}{m(\mathbf{x}_j)} \\ -\frac{M_z}{m(\mathbf{x}_i)} & -\frac{M_z}{m(\mathbf{x}_j)} \end{bmatrix} \quad (42)$$

where the influence function $\underline{w} \langle \boldsymbol{\xi}_{ij} \rangle$ used for the coupling bonds should be specified as $\underline{w} = 1$.

3.3. Coupling of the solid and fluid

This section describes the coupling process in planar conditions. In a plane discretization, see Fig. 5, the solid portion is discretized by PD nodes and the fluid portion is discretized by 4-node FE element. PD nodes and FE nodes share the same node coordinates. A bidirectional interaction between solid and liquid discretization is realized to link the local and non-local equations (Eqs.(34) and (41)). The same shape functions are used for generating the coupling matrix and the other fluid matrices, which are defined in terms of the normalized natural domain (i.e. $-1 \leq \xi \leq 1$ and

$-1 \leq \eta \leq 1$) and four Gauss points are used in the numerical integration.

$$\mathbf{N}_u = \mathbf{N}_p \Rightarrow \begin{cases} N_1 = \frac{1}{4} (1 - \xi) (1 - \eta) \\ N_2 = \frac{1}{4} (1 - \xi) (1 + \eta) \\ N_3 = \frac{1}{4} (1 + \xi) (1 + \eta) \\ N_4 = \frac{1}{4} (1 + \xi) (1 - \eta) \end{cases} \quad (43)$$

As shown in Fig. 6(a), let us consider a plate notched by a T-shaped crack with a fluid injection at the point Q of the horizontal crack. Under the action of the pore pressure, the solid skeleton deforms gradually. In Fig. 6(a), the initial mesh is grey and the deformed mesh is blue, at the meantime, the initial position of the nodes are represented by grey particles and the blue particles are the deformed position. To use Eq.(33) to evaluate the permeability coefficient in the crack domain, the aperture values at the PD nodes near crack surfaces need to be calculated. Here we choose two representative nodes as reference to explain the procedure for calculating the aperture values. As shown in Figs. 6(b) and 6(c), the magenta node is the current PD node marked as NODE i , while the nodes in its neighborhood that need to be used to calculate the aperture value at NODE i are marked as NODES j ($m_{ratio} = 2$). The right part of Figs. 6(b) and 6(c) are showing the relative position changes of NODES j to NODE i . The relative positions of NODE i and of one of the NODES j can be shown as in Fig. 7. The relative displacement vector η_{ij} as in Fig. 7 can be decomposed into two components: along and perpendicular to the direction of the original bond supposing that they represent the opening displacement and the dislocation of the crack, respectively. Hence the aperture value related to the bond ξ_{ij} can be expressed geometrically as:

$$a_{ij} = \|\xi_{ij}\|^d \cos \beta_{ij} - \|\xi_{ij}\|^o \quad (44)$$

The decomposition of the relative displacement vector can avoid updating the permeability coefficients at closed cracks with dislocations and can also reduce the error in updating the permeability coefficients at opening cracks with non negligible dislocations (see the bonds ξ_{ij_2} , ξ_{ij_3} in Fig. 6(c) and ξ_{ij_5} , ξ_{ij_7} in Fig. 6(b)). The computational procedure to evaluate the aperture value of NODE i is presented in Algorithm 1. The algorithm considers all broken bonds connected with NODE i and, for each of them, evaluates the aperture in the initial direction of the bond. Then, the aperture of the node is the average of bond apertures. Subsequently, the permeability and storage coefficients related to NODE i are updated correspondingly. Although this method may be improved, it is found in the subsequent applications to provide reasonable results.

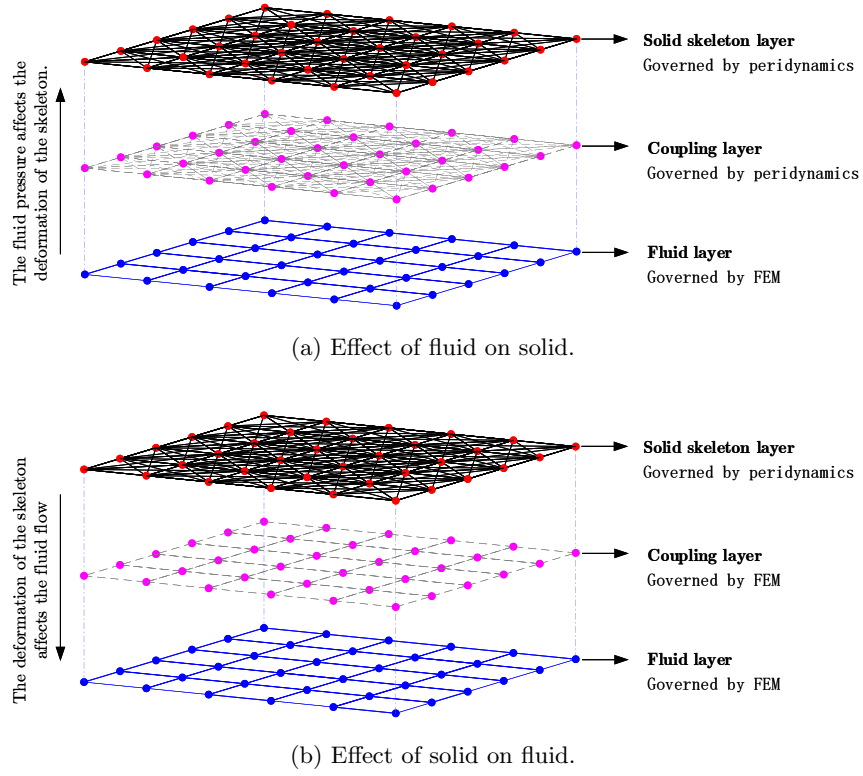


Figure 5: Schematic diagram of bidirectional influence in the coupling process.

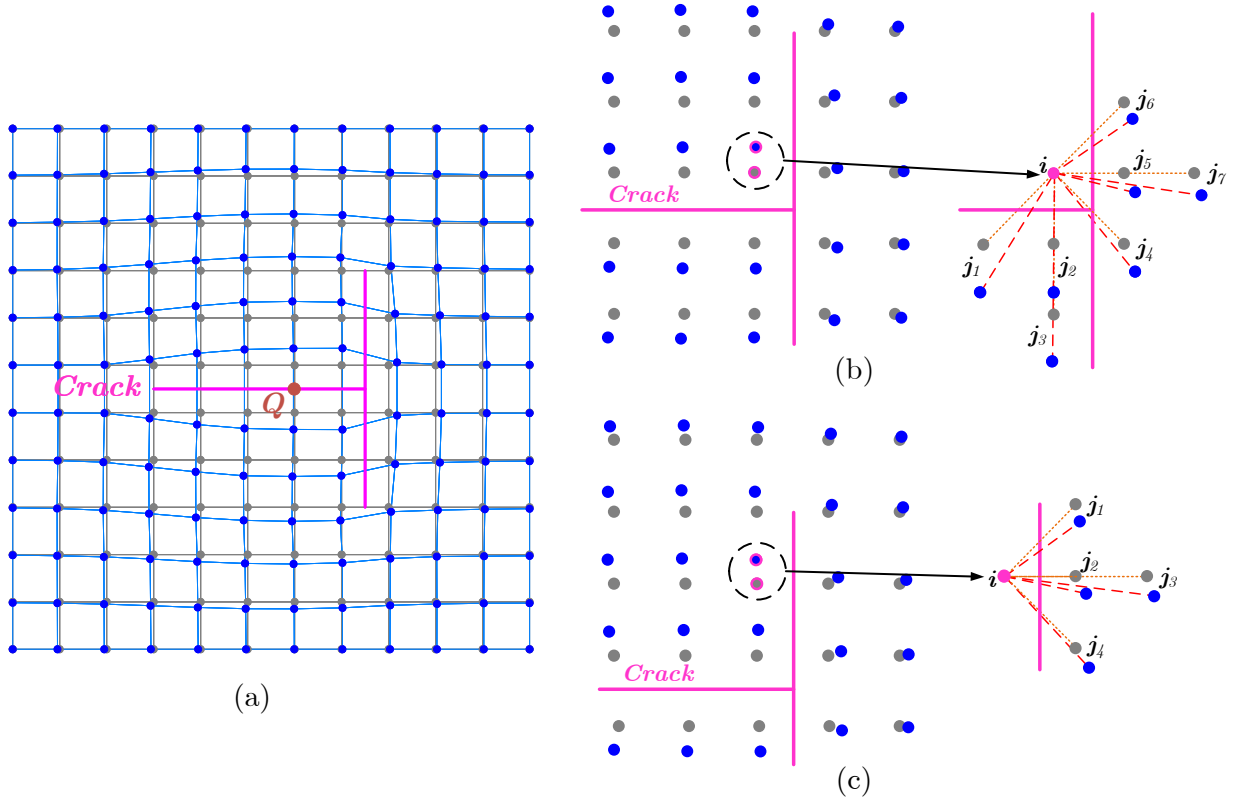


Figure 6: Schematic diagram for the calculation of the aperture value at PD node.

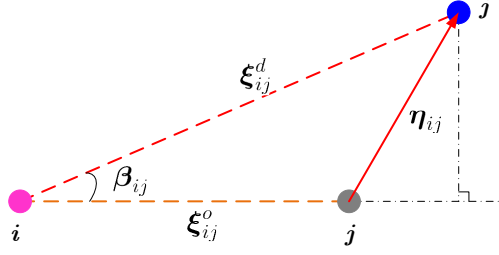


Figure 7: The decomposition of the relative displacement vector along and perpendicular to the direction of the original bond.

Algorithm 1: Routine for computing aperture value at the NODE i .

Input: $\|\xi_{ij}\|^o$, $\|\xi_{ij}\|^d$, β_{ij}

Output: a_i

- 1 $\|\xi_{ij}\|^o$ is the original length of bonds ξ_{ij} ;
 - 2 $\|\xi_{ij}\|^d$ is the deformed length of bonds ξ_{ij} ;
 - 3 β_{ij} is the angle between the initial bond and the deformed bond;
 - 4 a_i is the aperture value of NODE i ;
 - 5 n is a cumulative indicator ;
 - 6 Initialisation of n : $n = 0$, and a_i : $a_i = 0$;
 - 7 **for all bonds do**
 - 8 **if** $\frac{\|\xi_{ij}\|^d - \|\xi_{ij}\|^o}{\|\xi_{ij}\|^o} \geq s_c$ **and** $(\|\xi_{ij}\|^d \cos \beta_{ij}) - \|\xi_{ij}\|^o \geq 0$ **then**
 - 9 $a_i = a_i + (\|\xi_{ij}\|^d \cos \beta_{ij}) - \|\xi_{ij}\|^o$;
 - 10 $n = n + 1$;
 - 11 **end**
 - 12 **end**
 - 13 $a_i = a_i/n$;
-

3.4. Solution algorithms

To ensure the correctness and accuracy of the implementation of the PD-based hydraulic fracture model, transient consolidation and fluid flow problems are studied first. Thus, besides the algorithm for the solution of hydraulic fracturing problems, algorithms for transient consolidation analysis and transient fluid flow problems are also presented.

3.4.1. Algorithm for transient consolidation analysis

In transient consolidation problems, the inertia term governing the motion of the solid can be neglected [95], and Eqs.(34 and 42) are combined and rewritten as:

$$\begin{bmatrix} \mathbf{0} & \mathbf{0} \\ \mathbf{Q}^T & \mathbf{S} \end{bmatrix} \begin{bmatrix} \dot{\mathbf{u}} \\ \dot{\mathbf{p}} \end{bmatrix} + \begin{bmatrix} \mathbf{K}^{PD} & -\mathbf{Q}^{PD} \\ \mathbf{0} & \mathbf{H} \end{bmatrix} \begin{bmatrix} \mathbf{u} \\ \mathbf{p} \end{bmatrix} = \begin{bmatrix} \mathbf{f} \\ \mathbf{q}^w \end{bmatrix} \quad (45)$$

To solve the coupled system, the finite differences in time are used and the following expression is

reached [95]:

$$\begin{bmatrix} \vartheta \mathbf{K}^{PD} & -\vartheta \mathbf{Q}^{PD} \\ \mathbf{Q}^T & \mathbf{S} + \vartheta \Delta t \mathbf{H} \end{bmatrix}^{n+\vartheta} \begin{bmatrix} \mathbf{u} \\ \mathbf{p} \end{bmatrix}^{n+1} = \begin{bmatrix} (\vartheta - 1) \mathbf{K}^{PD} & (1 - \vartheta) \mathbf{Q}^{PD} \\ \mathbf{Q}^T & \mathbf{S} - (1 - \vartheta) \Delta t \mathbf{H} \end{bmatrix}^{n+\vartheta} \begin{bmatrix} \mathbf{u} \\ \mathbf{p} \end{bmatrix}^n + \begin{bmatrix} \mathbf{f} \\ \Delta t \mathbf{q}^w \end{bmatrix}^{n+\vartheta} \quad (46)$$

in which $0 \leq \vartheta \leq 1$ is the parameter for time integration.

3.4.2. Algorithm for transient fluid flow problem

Neglecting the coupling term caused by volumetric change in Eq.(34), the typical governing equation for fluid flow in saturated porous media can be expressed as:

$$\mathbf{S} \dot{\mathbf{p}} + \mathbf{H} \mathbf{p} = \mathbf{q}^w \quad (47)$$

To solve this equation, the following implicit time integration iteration is often used [101]:

$$\mathbf{p}^{n+1} = [\mathbf{S} + \vartheta \Delta t \mathbf{H}]^{-1} \{[\mathbf{S} - (1 - \vartheta) \Delta t \mathbf{H}] \mathbf{p}^n - \Delta t \mathbf{q}^w\} \quad (48)$$

In order to obtain a stable solution, ϑ is usually taken as $0.5 \leq \vartheta \leq 1$.

3.4.3. Algorithm for dynamic solution of hydraulic fracturing problems

Two classes of algorithms, “monolithic” and “staggered” are usually considered to solve the hydro-mechanical coupled system [102]. According to [95, 96, 100, 101], Eqs.(34) and (41) are combined and rewritten as:

$$\begin{bmatrix} \mathbf{M}^{PD} & \mathbf{0} \\ \mathbf{0} & \mathbf{0} \end{bmatrix} \begin{bmatrix} \ddot{\mathbf{u}} \\ \ddot{\mathbf{p}} \end{bmatrix} + \begin{bmatrix} \mathbf{0} & \mathbf{0} \\ \mathbf{Q}^T & \mathbf{S} \end{bmatrix} \begin{bmatrix} \dot{\mathbf{u}} \\ \dot{\mathbf{p}} \end{bmatrix} + \begin{bmatrix} \mathbf{K}^{PD} & -\mathbf{Q}^{PD} \\ \mathbf{0} & \mathbf{H} \end{bmatrix} \begin{bmatrix} \mathbf{u} \\ \mathbf{p} \end{bmatrix} = \begin{bmatrix} \mathbf{f} \\ \mathbf{q}^w \end{bmatrix} \quad (49)$$

which in concise form can be written as:

$$\mathbf{M} \ddot{\mathbf{a}} + \mathbf{C} \dot{\mathbf{a}} + \mathbf{K} \mathbf{a} = \mathbf{f} \quad (50)$$

The time integration of such system described in Eq.(50) can be carried out by using the “Truncated Taylor series collocation algorithm” presented in *sect.* 18.3.3 of [101]. A quadratic expansion is used (p=2). The solution of the unknown variable $\mathbf{a} = [\mathbf{u}, \mathbf{p}]^T$ at time step $n + 1$ is given by:

$$\mathbf{a}^{n+1} = -\mathbf{A}^{-1}(\mathbf{f}^{n+1} + \mathbf{C} \dot{\mathbf{a}}^{n+1} + \mathbf{M} \ddot{\mathbf{a}}^{n+1}) \quad (51)$$

where

$$\begin{aligned}
\mathbf{A} &= \frac{2}{\beta_2 \Delta t^2} \mathbf{M} + \frac{2\beta_1}{\beta_2 \Delta t} \mathbf{C} + \mathbf{K} \\
\dot{\mathbf{a}}^{n+1} &= -\frac{2\beta_1}{\beta_2 \Delta t} \mathbf{a}^n + \left(1 - \frac{2\beta_1}{\beta_2}\right) \dot{\mathbf{a}}^n + \left(1 - \frac{\beta_1}{\beta_2}\right) \ddot{\mathbf{a}}^n \\
\ddot{\mathbf{a}}^{n+1} &= -\frac{2}{\beta_2 \Delta t^2} \mathbf{a}^n - \frac{2}{\beta_2 \Delta t} \dot{\mathbf{a}}^n - \frac{1-\beta_2}{\beta_2} \ddot{\mathbf{a}}^n
\end{aligned} \tag{52}$$

in which $\beta_2 \geq \beta_1 \geq 0.5$ are parameters for the time integration.

However, when solving hydraulic fracturing problems by means of a “monolithic” approach, the system matrix needs to be updated in each step, and in addition, the combined system matrices will also be large, which will render the problem memory- and time-intensive. Therefore, another alternative option, the “staggered approach”, is adopted here. In [1], a “staggered coupling scheme” is implemented in COMSOL to solve the HF problems by using the phase-field model for saturated porous media. In each time step, the following solving scheme is adopted: the fields of pore pressure and displacement are calculated at first, then the historic strain field is updated according to the output pore pressure and displacement fields, whereafter the damage field is solved by using the fields already obtained. In addition, the Newton-Raphson algorithm is adopted in each staggered solution sequence, and a global relative error is estimated to determine whether to start a new iteration step or perform next time step. However, although the “staggered coupling scheme” in [1] can ensure the convergence of the coupled system, it seems to lose the ability to express some peculiar phenomena of the pore pressure, especially in dynamics. In this paper, at the expense of some robustness, a modified “staggered approach” is adopted to capture the hydrodynamic phenomena such as pore pressure oscillations in the hydraulic fracturing process. In the adopted “staggered approach”, the coupled system is divided into two parts, hydraulic diffusion and hydro-driven deformation of the porous solid [51, 52, 53], which means that the first row and second row of Eq.(49) are solved sequentially, and the previously solved results of \mathbf{u} and \mathbf{p} are used to evaluate the fluid volumetric source terms or nodal forces for the next solving sequence. In each solution sequence, there are two steps:

–step 1: solve the pressure field (\mathbf{p}^{n+1}) using the following implicit time integration iteration:

$$\mathbf{p}^{n+1} = [\mathbf{S} + \vartheta \Delta t \mathbf{H}]^{-1} \{[\mathbf{S} - (1 - \vartheta) \Delta t \mathbf{H}] \mathbf{p}^n - \Delta t \mathbf{q}^w + \mathbf{Q}^T (\mathbf{u}^n - \mathbf{u}^{n-1})\} \tag{53}$$

–step 2: solve the displacement field (\mathbf{u}^{n+1}) of the solid domain using the adaptive dynamic relaxation method presented in [79, 81].

In addition, if there are initial or propagating cracks in the porous media, the permeability and storage matrices (\mathbf{H} and \mathbf{S}) need to be updated accordingly in each time step. The flow chart of the solution algorithm by using the described “staggered approach” for HF problems is shown in Fig.8.

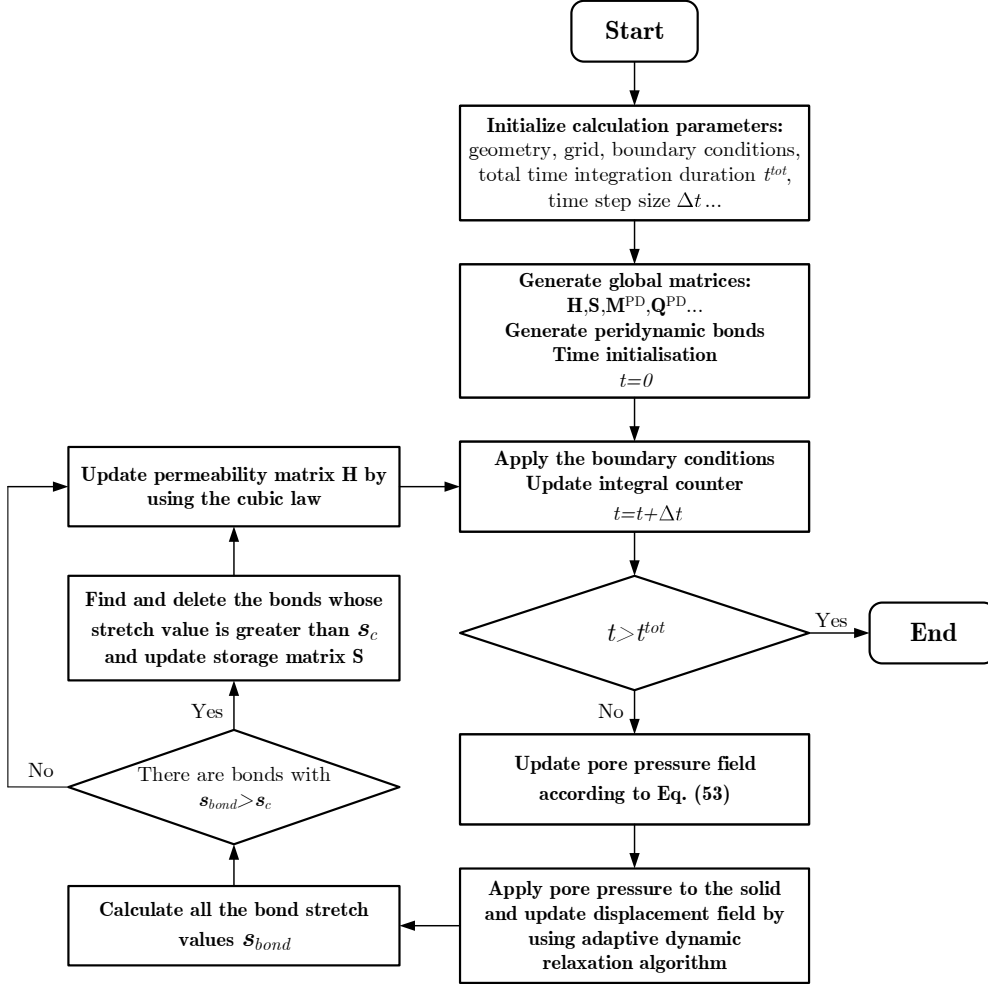


Figure 8: Flow chart of the solution algorithm for hydraulic fracture problems.

4. Numerical examples

In this section, several numerical examples are presented to demonstrate the capabilities of the proposed method. All examples are performed in plane strain conditions. The m -ratio is always taken as $m_{ratio} = 3$. First we show in Fig. 9 the distribution of damage value at the crack tip in a discrete peridynamic model. As shown in Fig. 9a, the nodes where damage values are greater than 0 can be divided into three types A, B and C. The damage value at nodes of type A is greater than 0.4, see Fig. 9b, while the value at nodes of type B is greater than 0.2. According to this characteristic, the threshold values are set as $c_1 = 0.2$ and $c_2 = 0.35$ in the linear indicator functions. Only one layer of elements would be identified in the fracture domain, which can minimize the influence sphere of the crack on the permeability parameters of elements. The smooth transition from fracture domain to reservoir domain is guaranteed by identifying the second layer of nodes in the transition domain. In addition, c_1 can also take other values smaller than 0.2.

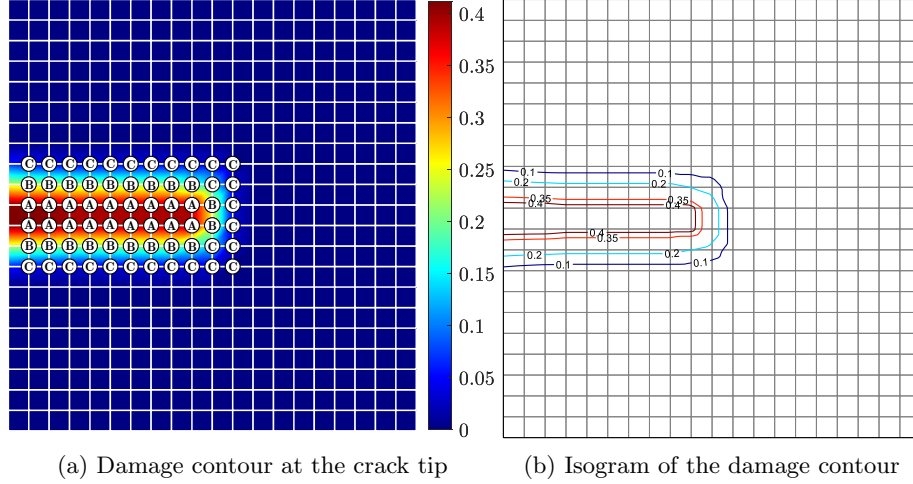


Figure 9: Damage value distribution at the crack tip in a discrete peridynamic model.

4.1. One-dimensional consolidation problem

We solve an one-dimensional consolidation problem presented in [74]. The material parameters are, Young modulus: $E = 10^8 Pa$, Poisson's ratio: $\nu = 0$, Biot constant: $\alpha = 0.5$, permeability coefficient: $k = 10^{-12} m^2$, fluid viscosity: $\mu^w = 10^{-3} Pa \cdot s$, storage coefficient: $S = 1 / (6.06 \times 10^9 Pa)$. Fig. 10 shows the geometry and boundary conditions. The analytical solutions of this problem are given as [74, 103]:

$$p(x, t) = \frac{4vP_0}{\pi} \sum_m^N \left\{ \frac{1}{2m+1} \exp \left(- \left(\frac{(2m+1)\pi}{2L} \right)^2 ct \right) \times \sin \left(\frac{(2m+1)\pi x}{2L} \right) \right\} \quad (54)$$

$$u(x, t) = c_m v P_0 \left\{ L - x - \frac{8L}{\pi^2} \sum_m^N \left\{ \frac{1}{(2m+1)^2} \exp \left(- \left(\frac{(2m+1)\pi}{2L} \right)^2 ct \right) \times \cos \left(\frac{(2m+1)\pi x}{2L} \right) \right\} \right\} + bP_0 (L - x) \quad (55)$$

in which $a = 10^{-8} Pa$, $b = \frac{a}{1+a\alpha^2/S}$, $v = \frac{a-b}{a\alpha}$, $c = \frac{\kappa}{(a\alpha^2+S)\mu_w}$ and $c_m = \frac{a-b}{v}$.

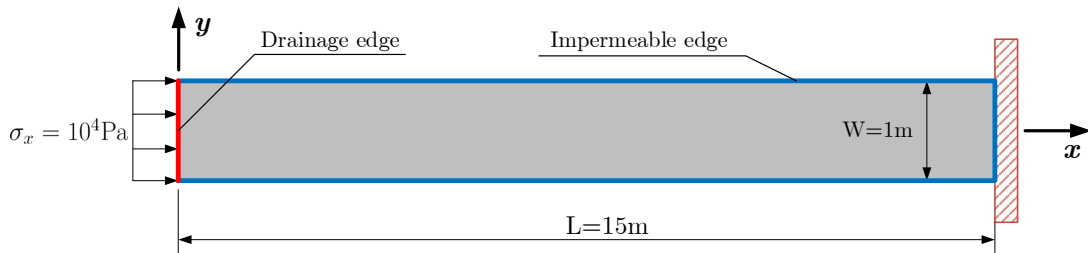


Figure 10: Geometry and boundary conditions of the consolidation problem.

The discretization parameters are horizon $\delta = 0.15m$, and the corresponding grid spacing is $\Delta x = \delta/m_{ratio} = 0.05m$. The solution algorithm in *sect.* 3.4.1 is used to solve this coupled system, and the time step is taken as $\Delta t = 1s$. Figs. 11 and 12 show the distributions of the pore pressure and displacement along the central axis at different times: 20s, 40s, 60s, 80s and 100s. The same problem has also solved by using a coupled peridynamic-only model presented in [74]. The numerical and analytical solutions are plotted in Figs. 11 and 12. Tab. 1 shows the computing costs of FEM/PD and PD-only solutions (PDM). The comparisons in Figs. 11 and 12 indicate that the results obtained by the proposed method are in excellent agreement with the analytical solutions, and the FEM/PD model has a higher efficiency than a PD-only model.

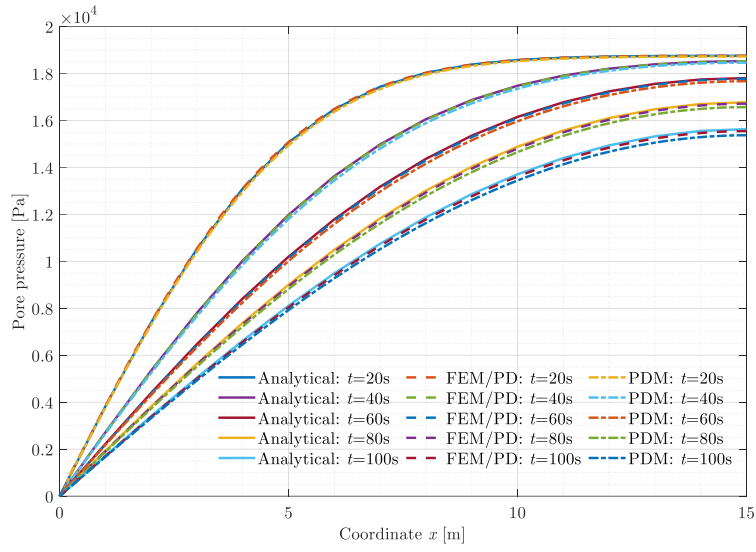


Figure 11: Comparison of analytical and PD pore pressure solutions along the central axis.

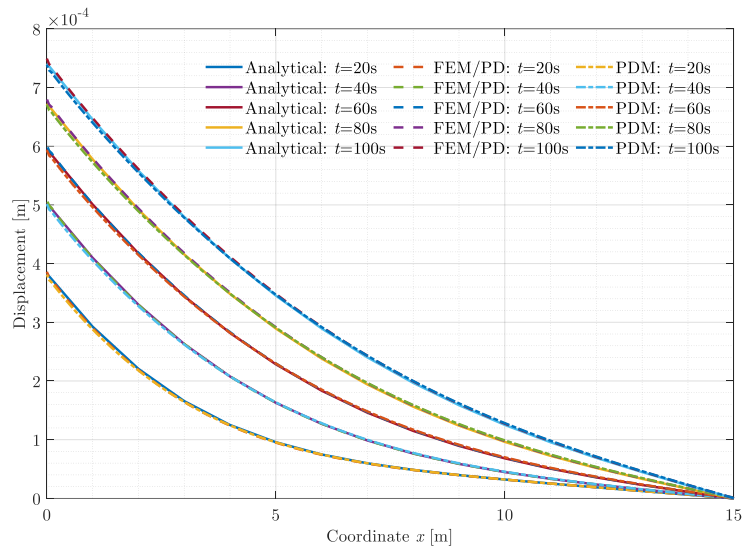


Figure 12: Comparison of analytical and PD displacement solutions along the central axis.

Table 1: Computing costs of the consolidation problem by using different methods.

Methods	FEM/PD	PD-only
CPU time [s]	37.69	62.85

4.2. Pressure distribution in a single crack

In this section, an example of variation of hydraulic pressure distribution with time in a single crack [1, 51] is studied by using the present method. Geometry and boundary conditions are shown in Fig. 13.

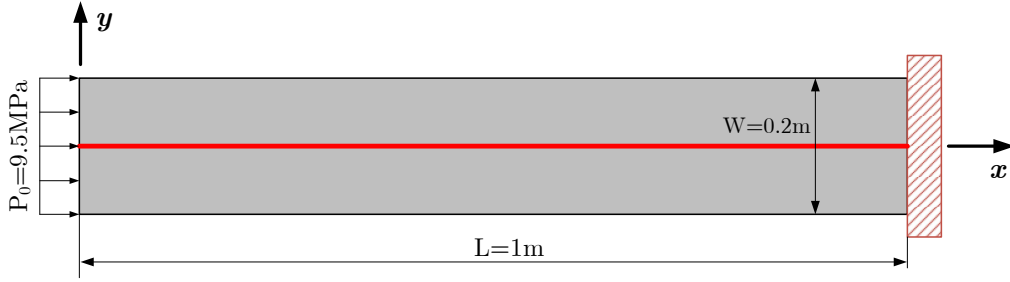


Figure 13: Geometry and boundary conditions for a rock sample with a single crack.

A hydraulic pressure $P_0 = 9.5MPa$ is applied suddenly on the left edge, while the other edges are impermeable. This is an "unsteady" or evolving problem, and its analytical solution available in [1] is given as:

$$\frac{P}{P_0} = 1 + \frac{4}{\pi} \sum_{n=0}^{\infty} \left[\exp\left(- (2n+1)^2 (T/4) \pi^2\right) \cos\left(\frac{(2n+1)\pi}{2} \zeta\right) \left(\frac{(-1)^{n+1}}{2n+1}\right) \right] \quad (56)$$

in which $\zeta = \frac{L-x}{L}$, P is the pressure value at x , L is the length of the specimen, and T_d is a dimensionless time, defined as:

$$T_d = K_w \frac{(a^2/(12\mu_w)) t}{L^2} \quad (57)$$

where K_w and μ_w are the bulk modulus and viscosity coefficient of the fluid, and a is the aperture of the central crack. To compare with the analytical solution, we only solve the fluid flow part by using the solution algorithm in *sect.3.4.2*. The parameters associated to the fluid flow are taken as: $K_w = 2.2GPa$, $\mu_w = 10^{-3}Pa \cdot s$, $\alpha = 1$, $n = 2 \times 10^{-5}$ and $a = 3 \times 10^{-5}m$. Two sets of discretization parameters have been used as a comparison: horizon $\delta_1 = 15mm$ and $\delta_2 = 30mm$, the corresponding grid spacings are $\Delta x = \delta_1/m_{ratio} = 5mm$ and $\Delta x = \delta_2/m_{ratio} = 10mm$. The initial crack is described

by the peridynamic portion and the FEM model for the calculation of the fluid flow is modified accordingly. The time integration parameters are taken as: $\Delta t = 2 \times 10^{-8} s$ and $\vartheta = 0.5$.

Figs. 14a to 14d show the comparison between the numerical and analytical solutions of the pressure distributions along the initial crack at different times T_d . The relative differences between the numerical and analytical solutions are plotted in Fig. 15. In general, the numerical solutions are very close to the analytical ones and a denser grid generate a more accurate solution.

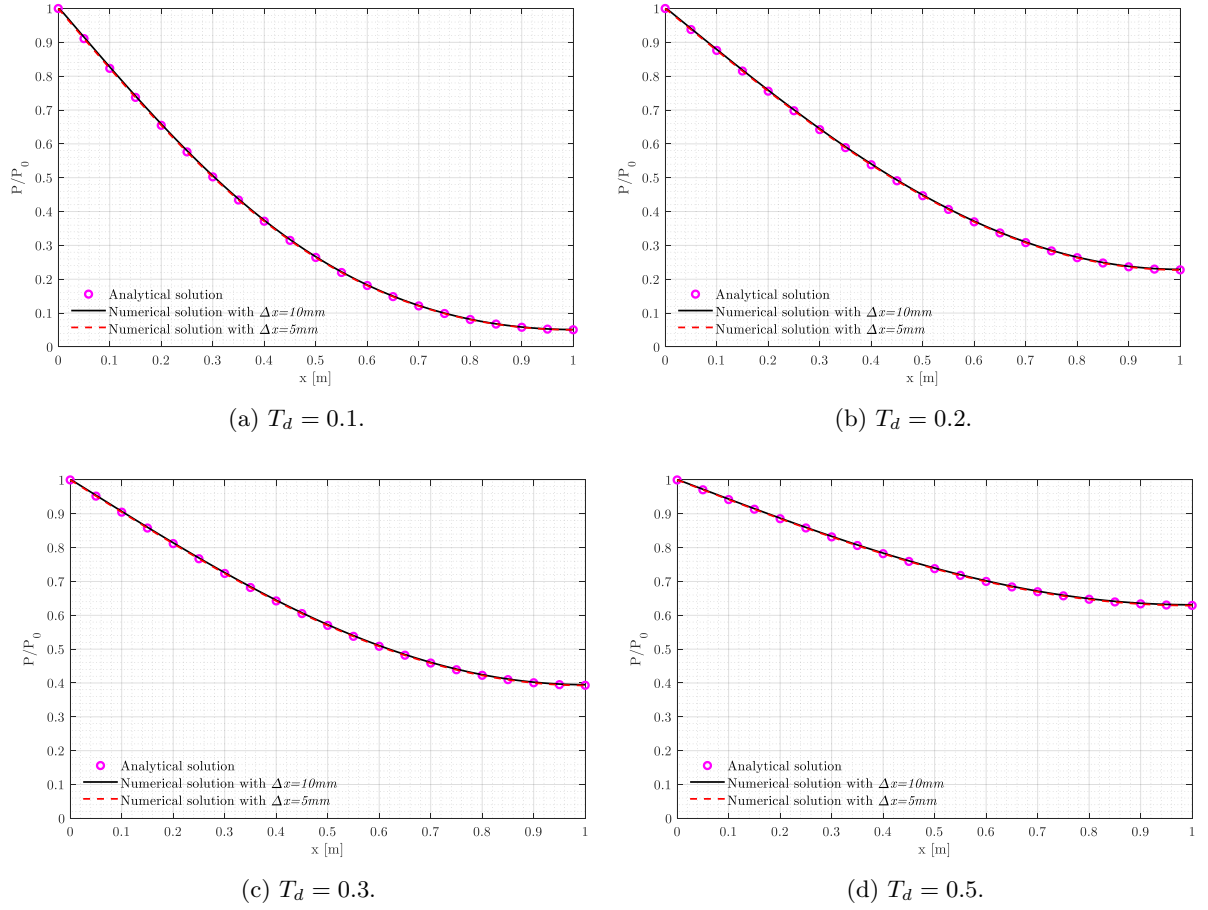


Figure 14: Comparison of the numerical and analytical pressure distribution along the crack.

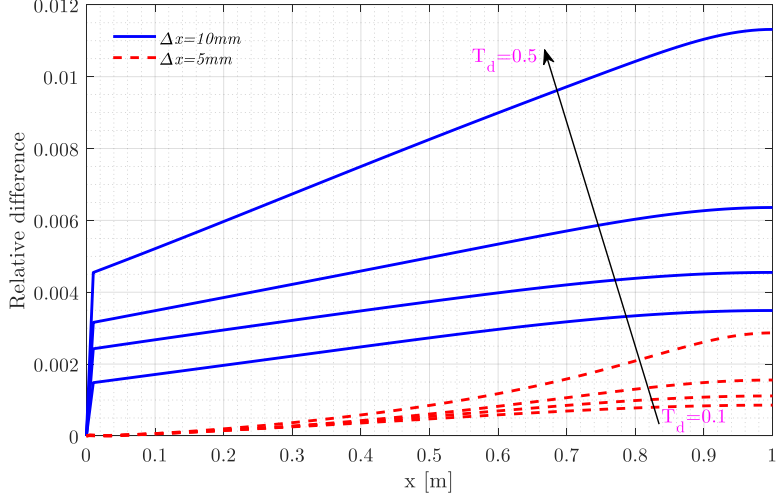


Figure 15: The relative differences between numerical and analytical solutions of the pressure distribution along the single crack.

4.3. Pressure-driven fracture propagation: a centrally notched specimen subjected to an increasing internal pore pressure

In this section, a pressure-driven fracture propagation example presented in [2] is solved by applying the present method. Geometry and boundary conditions are shown in Fig. 16. An increasing pressure is applied on the surface of the initial crack to deform the specimen. Assume that the length of the initial crack is $2l_c$, the vertical displacement of the crack surface driven by the pore pressure can be given analytically as [2, 104]:

$$u(x, p) = \frac{2pl_c}{E_p} \left(1 - \frac{x^2}{l_c^2}\right)^{1/2} \quad (58)$$

in which $E_p = E/(1 - \nu^2)$ is the plane strain Young's modulus and E and ν are the Young's modulus and Poisson's ratio, respectively.

The mechanical and fluid parameters used in the calculation are, Young's modulus: $E = 210GPa$, Poisson's ratio: $\nu = 0.3$, critical energy release rate: $G_c = 2700J/m^2$, porosity: $n_r = 0.002$, mass density: $\rho_r = \rho_f = 1000kg/m^3$, biot constant: $\alpha = 1$, bulk modulus and viscosity coefficient of the fluid: $K_w = 10^8Pa$ and $\mu_w = 10^{-3}Pa \cdot s$, permeability coefficient of the reservoir domain: $k_r = 10^{-15}m^2$.

The whole domain is discretized with uniform quadrilateral grid. The FE nodes of the fluid mesh and the PD nodes of the solid grid have the same coordinates. Two sets of discretization parameters are taken for comparison: Mesh 1 with a size of $\Delta x_1 = 10^{-2}m$ and Mesh 2 with a size of $\Delta x_2 = 5 \times 10^{-3}m$.

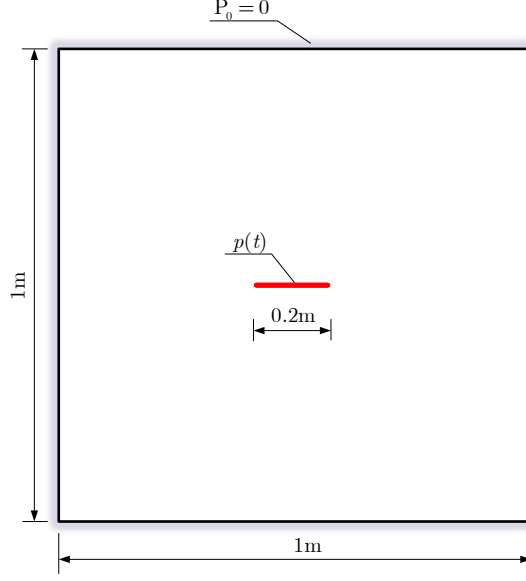


Figure 16: Geometry and boundary conditions of the notched specimen subjected to internal pressure.

The corresponding horizons are $\delta_1 = \Delta x_1 \times m_{ratio} = 3 \times 10^{-2}m$ and $\delta_2 = \Delta x_2 \times m_{ratio} = 1.5 \times 10^{-3}m$. As in [2], the pressure leading to crack propagation with the adopted parameters is about $60MPa$. Thus, the final pressure $60.5MPa$ is applied on the crack surface in 2200 uniform time steps, and each time step is divided into 2500 small incremental time steps with a size of $\Delta t = 4 \times 10^{-4}s$. Fig. 17 shows the comparison between the displacement along the notch of the present results and the analytical solution. The numerical results obtained with the denser mesh are closer to the analytical solutions than those obtained with sparser mesh, and they are all in good agreement. When the applied pressure reaches $59.235MPa$ at $2154s$, the crack starts to propagate. The variations of the crack pattern and the distribution of pressure are shown in Figs. 18a to 18f.

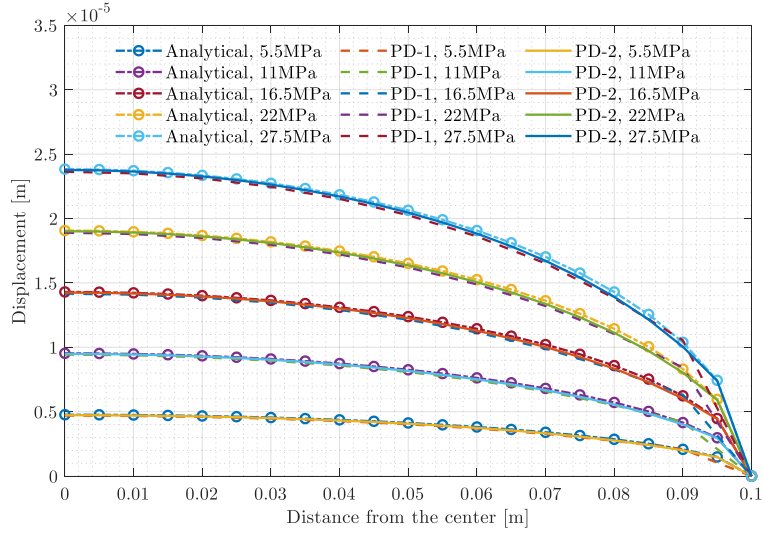


Figure 17: Comparison of the displacement along the notch between the present results and the analytical solution.

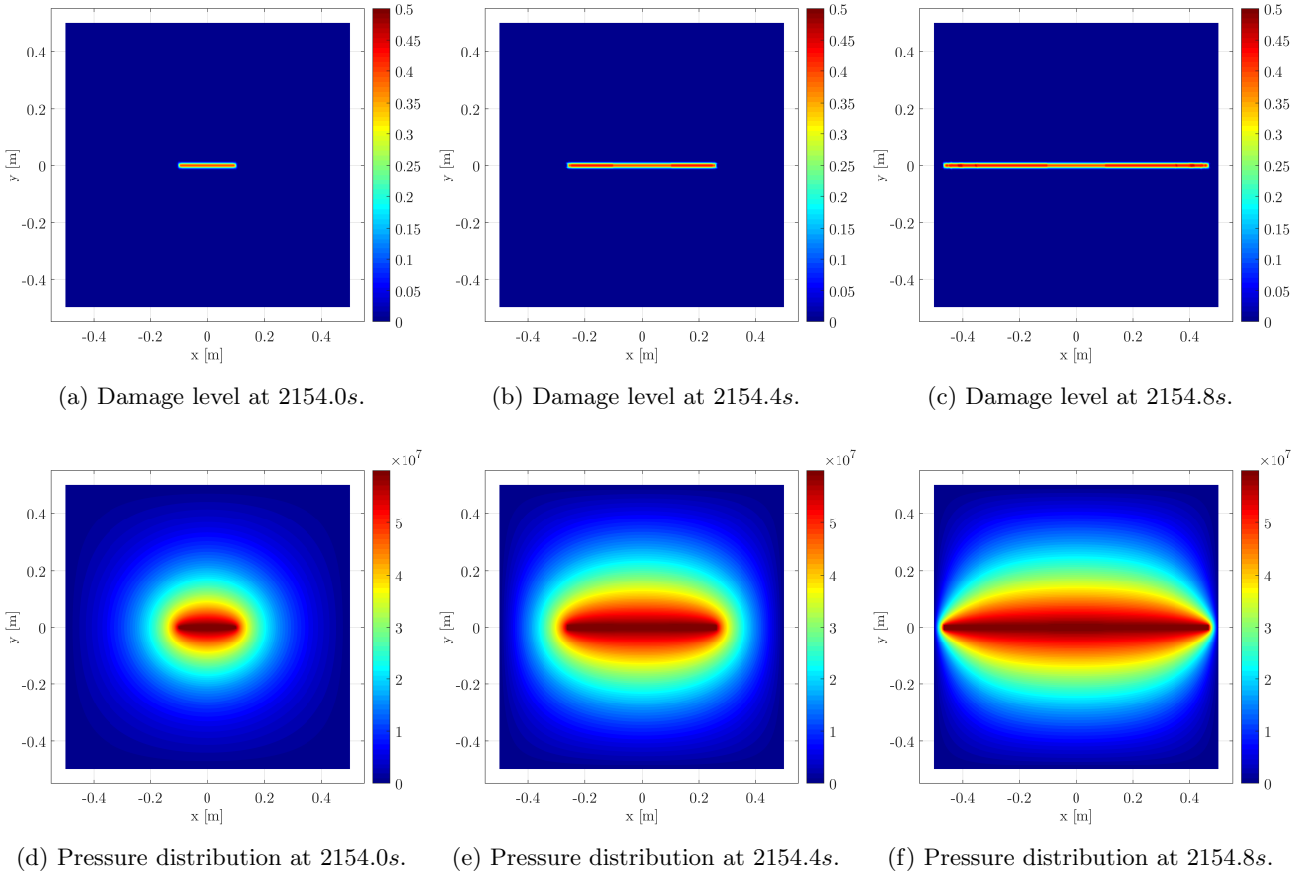


Figure 18: Crack propagation and the variation of pressure distribution at different time steps.

4.4. Fluid-driven fracture propagation: reproducing the results of the KGD model

In this example we deal with fluid driven fracture initiation and propagation. This is completely

different from the case of *sect. 4.2* where a pressure driven fracture is investigated. In that case the driving force is applied directly to the momentum balance equation of the mixture, Eq.(7), via the pressure term in the effective stress principle, Eq.(22), while in case of fluid driven fracture the loading term is applied to the fluid mass balance equation Eq.(28). Its effect is then transmitted to the momentum balance equation via the coupling terms. The loading cases for instance determine whether a power law behavior exists or is destroyed. This was clearly evidenced in [54]. In general the comparison of results for crack propagation between numerical models and exact solutions is not an easy task in fluid driven fracture. The reason is that the respective methods and underlying assumptions strongly impact the results. Exact solutions are based on many simplifying assumptions which are not always easy to implement in numerical methods based on more advanced approaches as explained below. Typical such assumptions are zero fluid lag, flow occurring predominantly in the fracture plane, finite and non-zero propagation speed, linear elastic fracture mechanics. They result in a steady propagation of a semi-infinite crack with constant or smoothly changing tip velocity [105, 106]. As far as LEFM is concerned, De Pater [107] states that “carefully scaled laboratory studies have revealed that conventional models for fracture propagation which are based on LEFM cannot adequately describe propagation. Instead, propagation should at least be based on tensile failure over a cohesive zone”.

Boone and Ingraffea [108] presented a FEM/FD model based on LEFM with a moving crack along a path known a priori. They assume negligible fracture toughness or fracture energy; further their procedure does not allow to specify flow at the crack mouth hence some iterations are needed in this case. These authors compare their solution with the analytical solution of Spence and Sharp [109] based on an approximation to an asymptotic solution; in particular the fluid is incompressible, the fracture impermeable and fluid lag in the tip region is excluded. Secchi et al. [13] with their FEM model based on cohesive tractions used the same analytical solution for a comparison, but had to introduce LEFM to obtain favourable results. They recovered however the stepwise advancement of the fracture tip, obviously not present in the analytical solution. Some results are shown below for comparison.

Baykin and Golovin [110] reduced for comparison reason their cohesive model to an elastic one with Biot coefficient $\alpha = 0$. Esfahani and Gracie [111] use XFEM with a cohesive model and drained/undrained split. They validate their model with respect to the solution for the problem of a planar hydraulic fracture (HF) that propagates under plane strain condition, presented by Geertsma and De Klerk [112], known as the KGD HF model. As Secchi et al. [13] they find that the KGD solution cannot be directly compared with the results of a cohesive HF model. The reason is that the KGD model is independent of the fracture energy (or, equivalently, fracture toughness), whereas

the solution of a cohesive HF model strongly depends on the value of the fracture energy and the length of the cohesive zone. The KGD solution represents the propagation of a plane strain HF in a viscosity dominated regime, whereas the solution of a cohesive HF gets close to a viscosity dominated regime only when its cohesive zone vanishes (or when the fracture toughness tends to zero). Therefore, the KGD and cohesive models are only comparable when the fracture propagates to such an extent that the cohesive zone is a negligible portion of the total fracture length, or when the fracture energy (fracture toughness) tends to zero. Finally, Chen et al. [113] use a Boundary Element Model with LEFM for modeling planar 3D hydraulic fracture growth. Their results compare well with analytical solutions but evidence stepwise fracture advancement as opposed to smooth behaviour.

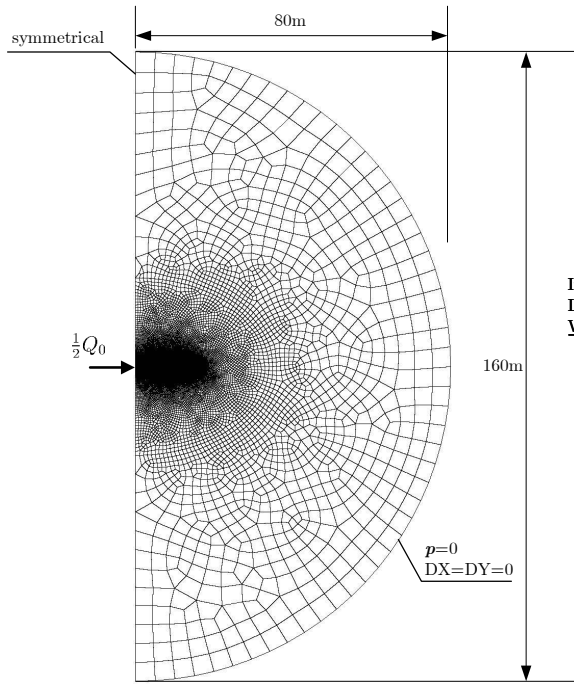
To assess the accuracy of the proposed method in case of fluid driven crack propagation we have simulated the case of Spence and Sharp [109], keeping in mind that different methods give different answer as just explained above i.e. with different constitutive models it is difficult to represent the so-called exact solutions. The problem is considered in plane strain conditions and the fluid is injected at the center of an initial crack with a constant injection rate of $Q_0 = 10^{-4}m^3/s$. The infinite medium is approximated as in Fig. 19a where the geometry and boundary conditions are shown, the grid size along the crack tip is $\Delta x = 0.05m$. The parameters used in the simulation are listed in Tab. 2. The fluid flow is governed by FEM only, the solid part is modeled by the coupling approach described in [59, 81], the global coupling matrix is generated by using a similar way, correspondingly.

Table 2: Mechanical and fluid parameters used in the reproduction of the KGD model.

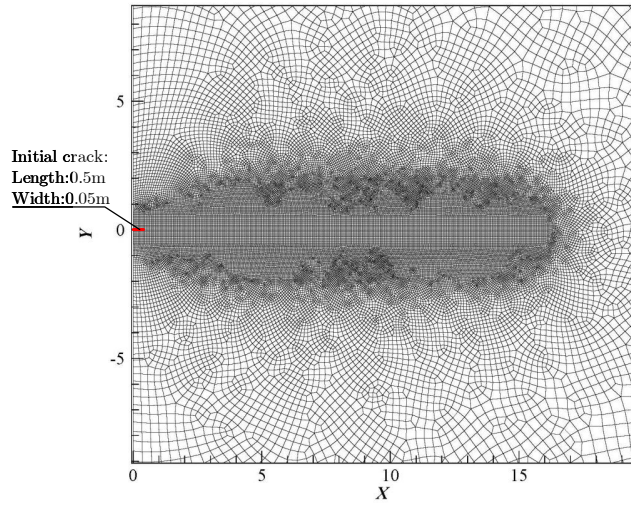
E	ν	G_c	ρ	α	n	K_w	μ	k
14.4GPa	0.2	10J/m ²	1000kg/m ³	0.7883	0.19	3GPa	10 ⁻³ Pa·s	2 × 10 ⁻¹⁴ m ²

The obtained results with the hybrid FEM/PD model are compared with the exact solution and with the results of the FEM solution of Secchi et al. [13] and Peruzzo et al. [100] in Figs. 20 to 22 for respectively crack mouth opening displacement, crack length and pressure at the injection point.

Given the difference in the adopted constitutive models the results are acceptable. In particular the stepwise crack tip advancement with irregular steps is recovered. This shows that the hybrid FEM/PD method is able to represent experimentally observed features, which are rather difficult to reproduce. Fewer crack advancement steps in a time interval than the number of time steps as in Fig. 21 is a reliable indicator that the behavior is truly stepwise. The stepwise advancement has been explained by Biot’s theory in [54]. A further explanation can be borrowed from Huang and Detournay [114] who obtained in a fracturing DEM model “plateaus” as in Fig. 21 and observe that “when the crack is temporarily arrested, another sudden extension in the crack length occurs only after enough energy has been accumulated in the system”. The example also evidences the impact of the assumed

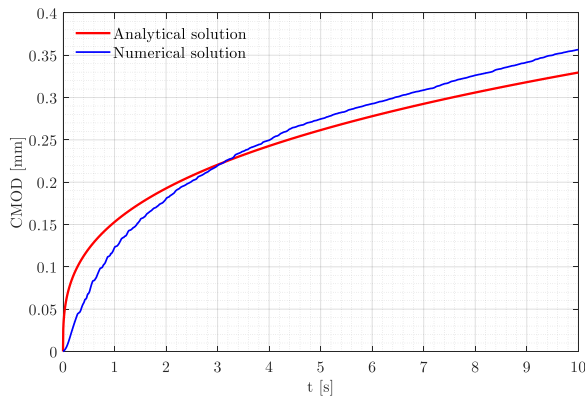


(a) Global geometry and mesh

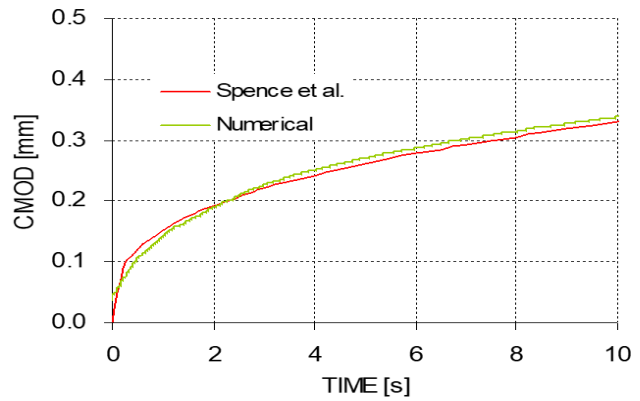


(b) Mesh around the preset crack propagating path

Figure 19: Diagrammatic sketch of the KGD model.



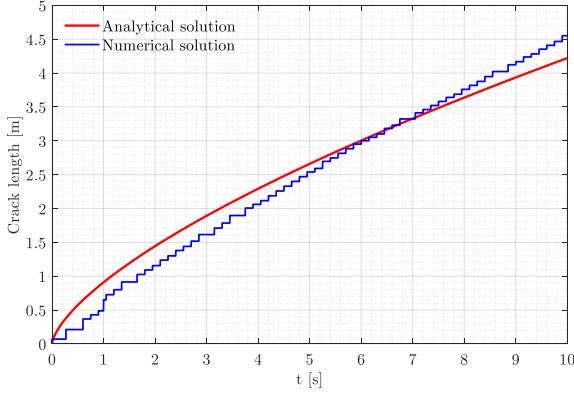
(a) The result of hybrid FEM/PD model.



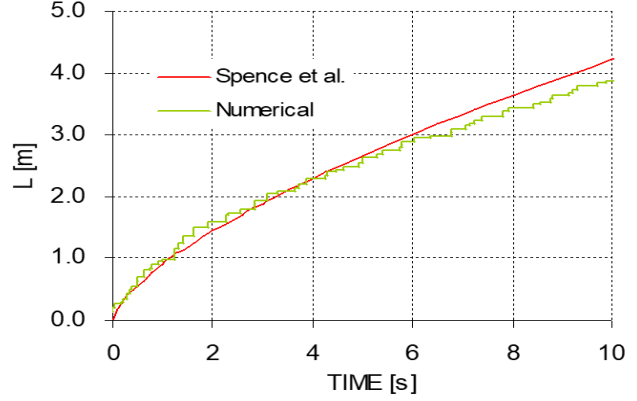
(b) The result reported in Secchi et al. 2007.

Figure 20: CMOD vs. time: (a) results obtained by FEM/PD model ($\Delta t = 10^{-3}s$); (b) results from [13] obtained by FEM model with LEFM ($\Delta t = 10^{-2}s$), redrawn with permission from Secchi et al. 2007.

solid behaviour in HF modelling.

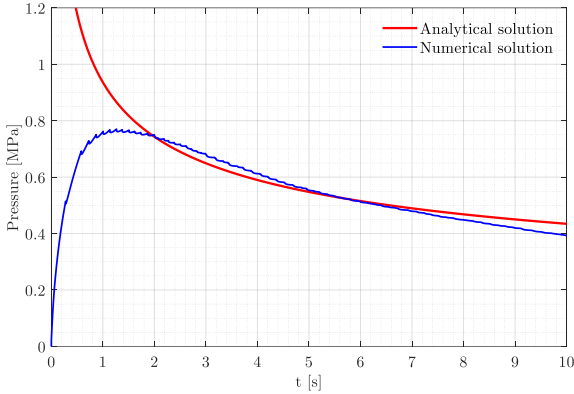


(a) The result of hybrid FEM/PD model.

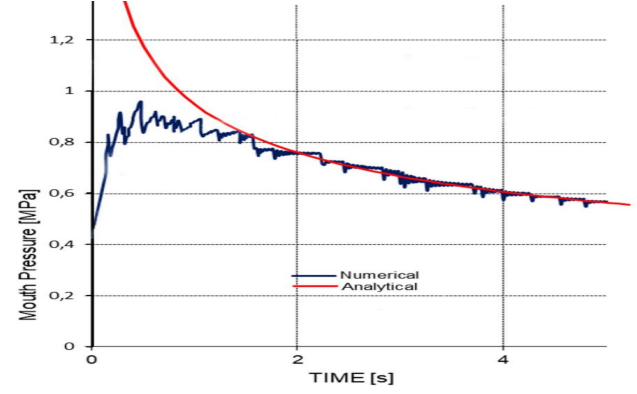


(b) The result reported in Secchi et al. 2007.

Figure 21: Crack length vs. time: (a) results obtained by FEM/PD model ($\Delta t = 10^{-3}s$); (b) results from [13] obtained by FEM model with LEFM ($\Delta t = 10^{-2}s$), redrawn with permission from Secchi et al. 2007. Note that the advancement steps in one sec are much less than the number of time steps. This is a reliable indication that the behaviour is truly stepwise.



(a) The result of hybrid FEM/PD model.



(b) The result reported in Peruzzo et al. 2019.

Figure 22: Pressure at the injection point vs. time: (a) results obtained by FEM/PD model; (b) results from [100] obtained by FEM model with LEFM , redrawn with permission from Peruzzo et al. 2019.

4.5. Fluid-driven fracture propagation: interaction between HF crack and natural cracks

In this section, three different fluid-driven fracture cases are studied to evidence the characteristics and capabilities of the present method. Geometric parameters and boundary conditions are shown in Fig. 23. Referring to [9], the mechanical and fluid parameters used in the calculations are shown in Tab. 3. In case 1, a crack is located at the center of the specimen with the initial length $l = 0.25m$, while in cases 2 and 3, additional vertical cracks with a length of $1m$ are set in the specimen to study the interaction between hydraulic cracks and pre-existing natural cracks. The fluid is injected at the center of the initial crack with a constant volume rate of $Q = 1 \times 10^{-3}m^3/s$. This and the following flow rates, together with the assumed dynamic viscosity, are in the range of high flow rate and low viscosity, investigated in [115]. The whole model is discretized using uniform quadrilateral elements for fluid flow with a grid size of $\Delta x = 1 \times 10^{-2}m$, while the PD grid shares the same node positions.

The corresponding horizon is $\delta = m_{ratio} \times \Delta x = 3 \times 10^{-2}m$. The time integral parameters are taken as: $\Delta t = 1 \times 10^{-3}s$ and $\vartheta = 1$.

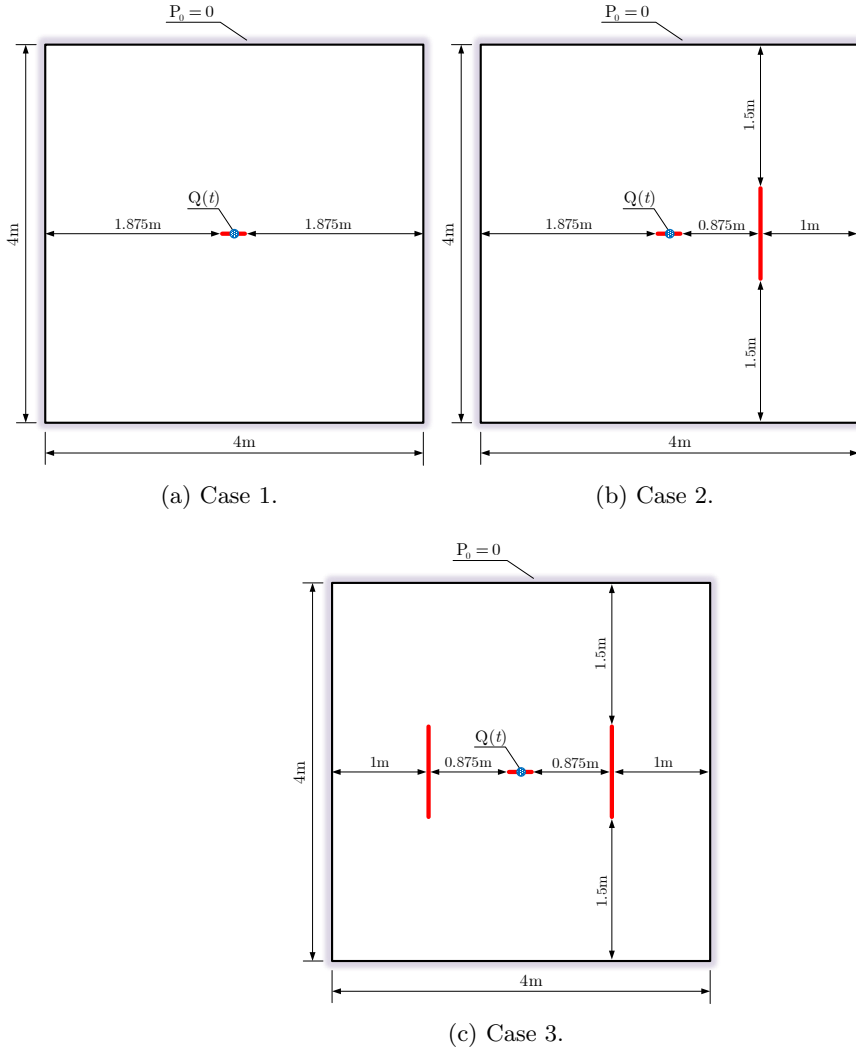


Figure 23: Geometry and boundary conditions of the notched specimens subjected to internal fluid injection.

Table 3: Mechanical and fluid parameters used in fluid-driven fracture examples.

E	ν	G_c	ρ	α	n	K_w	μ	k
$10^8 Pa$	0.2	$100 J/m^2$	$1000 kg/m^3$	1	0.4	$10^8 Pa$	$10^{-3} Pa \cdot s$	$10^{-12} m^2$

The values of the pressure at the injection point are recorded in time and plotted in Fig. 24. As shown in the magnifying frame ① of Fig. 24, at the moment of injection, the pressure value at the injection point suddenly increases to a large value, under its action, the initial central crack opens gradually, and the permeability in the initial central crack domain increases correspondingly, which leads to a steep drop of the pressure. Shown at the right half part of Fig. 24, the fluid diffusion is isotropic because of the small crack opening width (see the pressure distribution at instant A).

With the increase of the crack opening width, the fluid diffusion takes precedence over crack direction (instant B), until the pressure values at the crack tips are approximately equal to that at the injection point (instant C). After instant C, hydraulic fracture occurs in all the cases, and the pressure values can rise a bit at the incipient stage because the crack propagates slowly, soon afterwards, hydraulic cracks propagate rapidly, the pressure values drop gradually. In cases 2 and 3, after the hydraulic cracks touch the natural vertical crack sets and force them to open, the pressure values suddenly drop at extreme speed (between instants D and E), afterwards, the pressure values in the vertical cracks increase gradually until the new cracks start to propagate from their tips and finally extend to the boundary of the specimen. After cracks touch the 0-pressure boundary of the specimen, the pressure value at the injection point drops again at an extreme rate (see the parts after the instant F in Fig. 24).

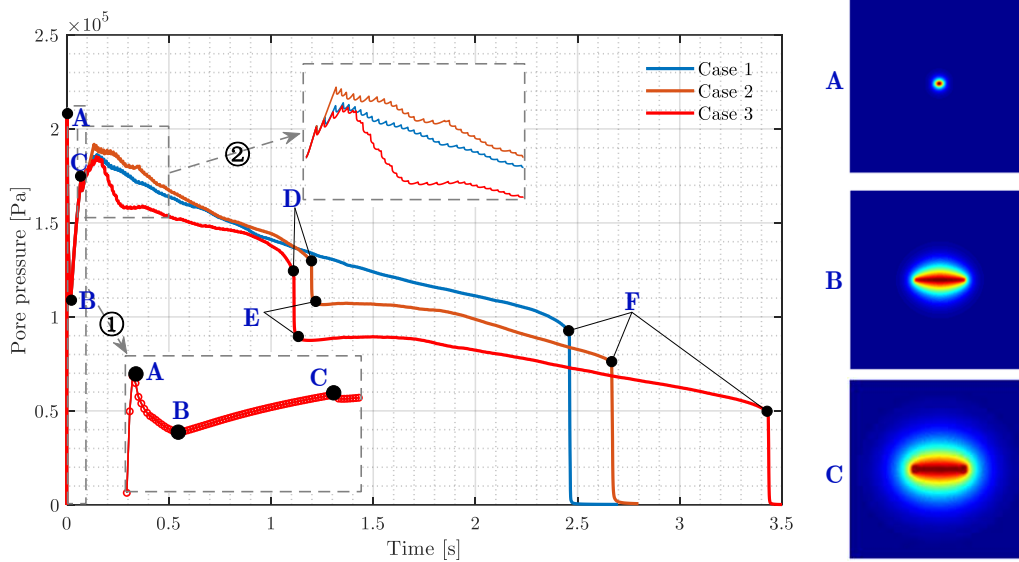


Figure 24: Variation of pressure value at injection point with time.

Figs. 25, 26 and 27 show the crack patterns and the corresponding variation of pressure distributions in cases 1, 2 and 3 at three different time instants during the fracturing process. With the injection of fluid, the injected fluid flows along the cracks and forces the fluid pressure near the crack area to increase, correspondingly, the solid skeleton deforms and crack propagates. The present method can describe the phenomena of spontaneous crack propagation and the fluid flow in fractured saturated porous media in a simple but reasonable way.

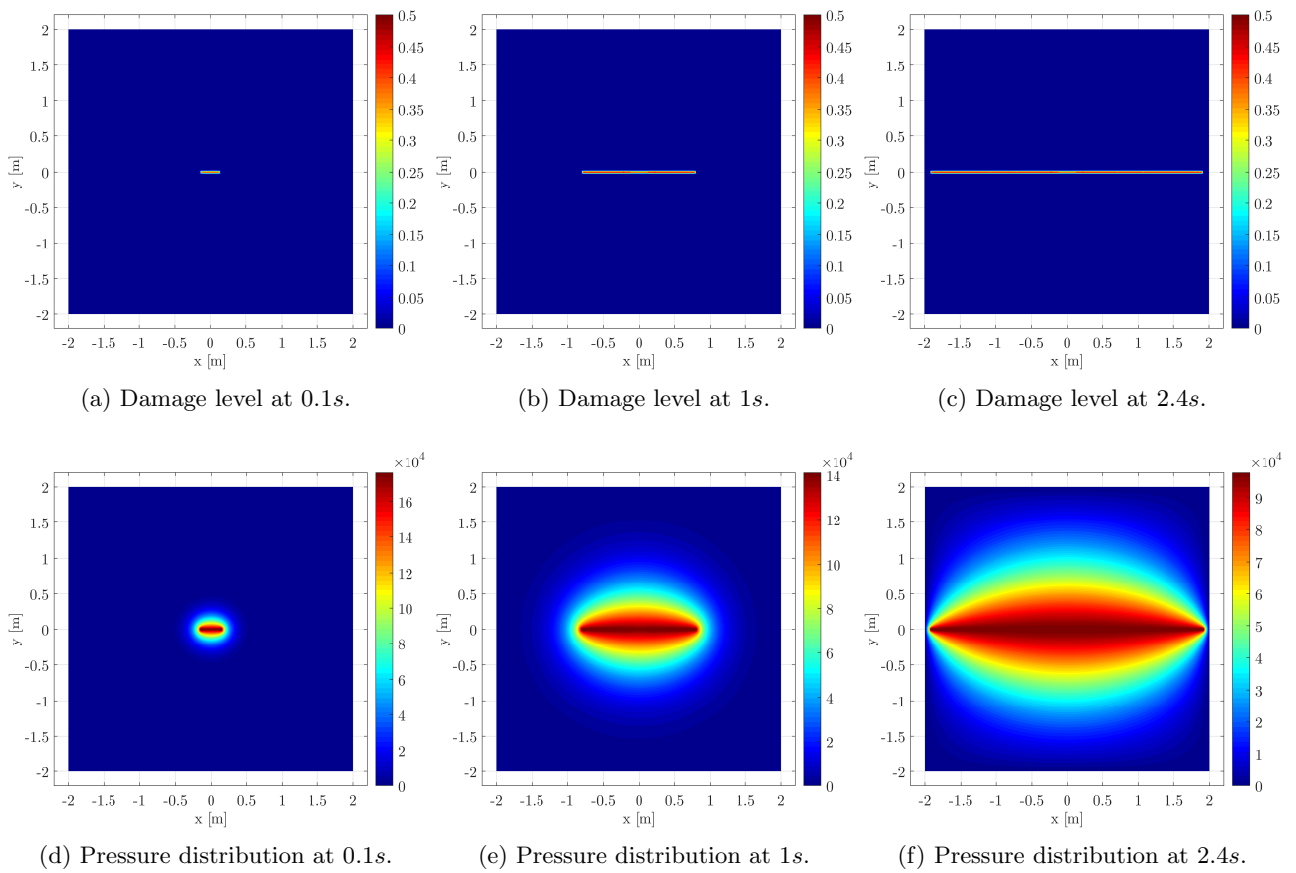
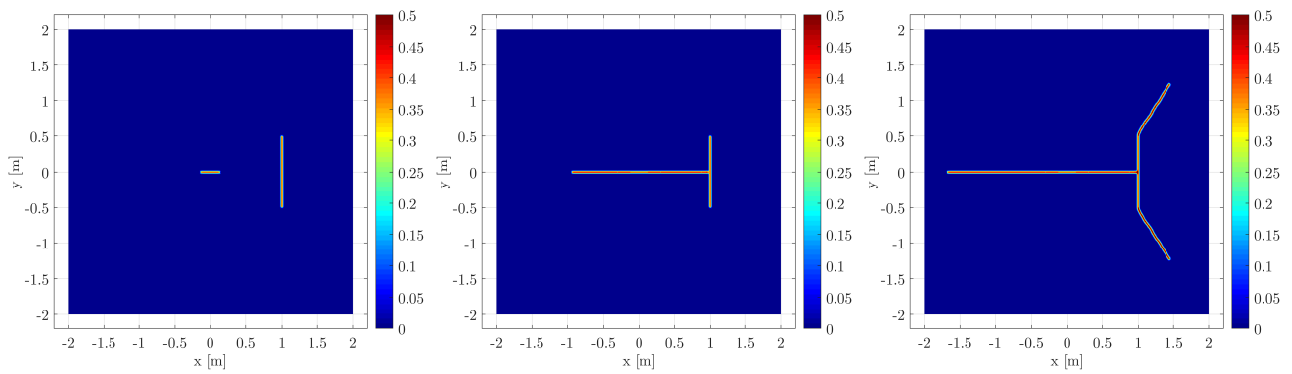


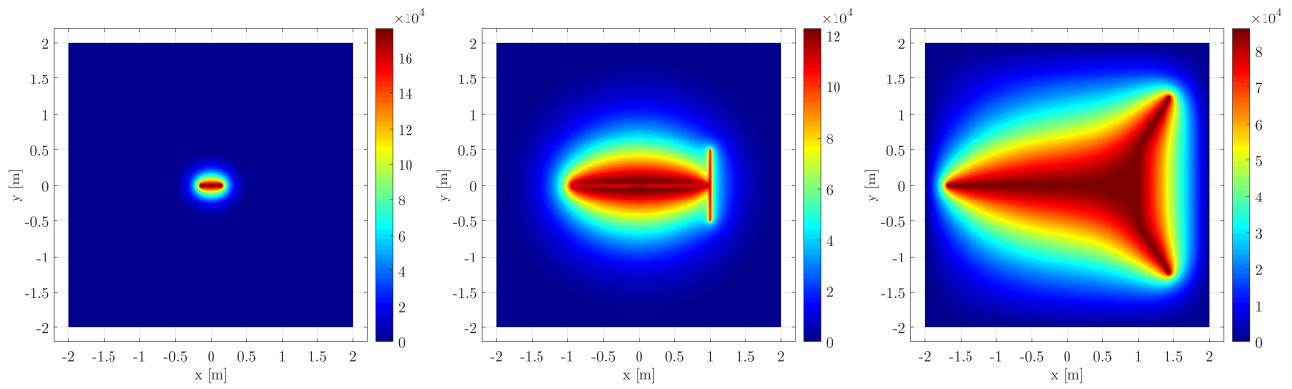
Figure 25: Crack propagation and variation of pressure distribution in case 1 at three time instants.



(a) Damage level at 0.1s.

(b) Damage level at 1.2s.

(c) Damage level at 2.4s.



(d) Pressure distribution at 0.1s.

(e) Pressure distribution at 1.2s.

(f) Pressure distribution at 2.4s.

Figure 26: Crack propagation and variation of pressure distribution in case 2 at three time instants.

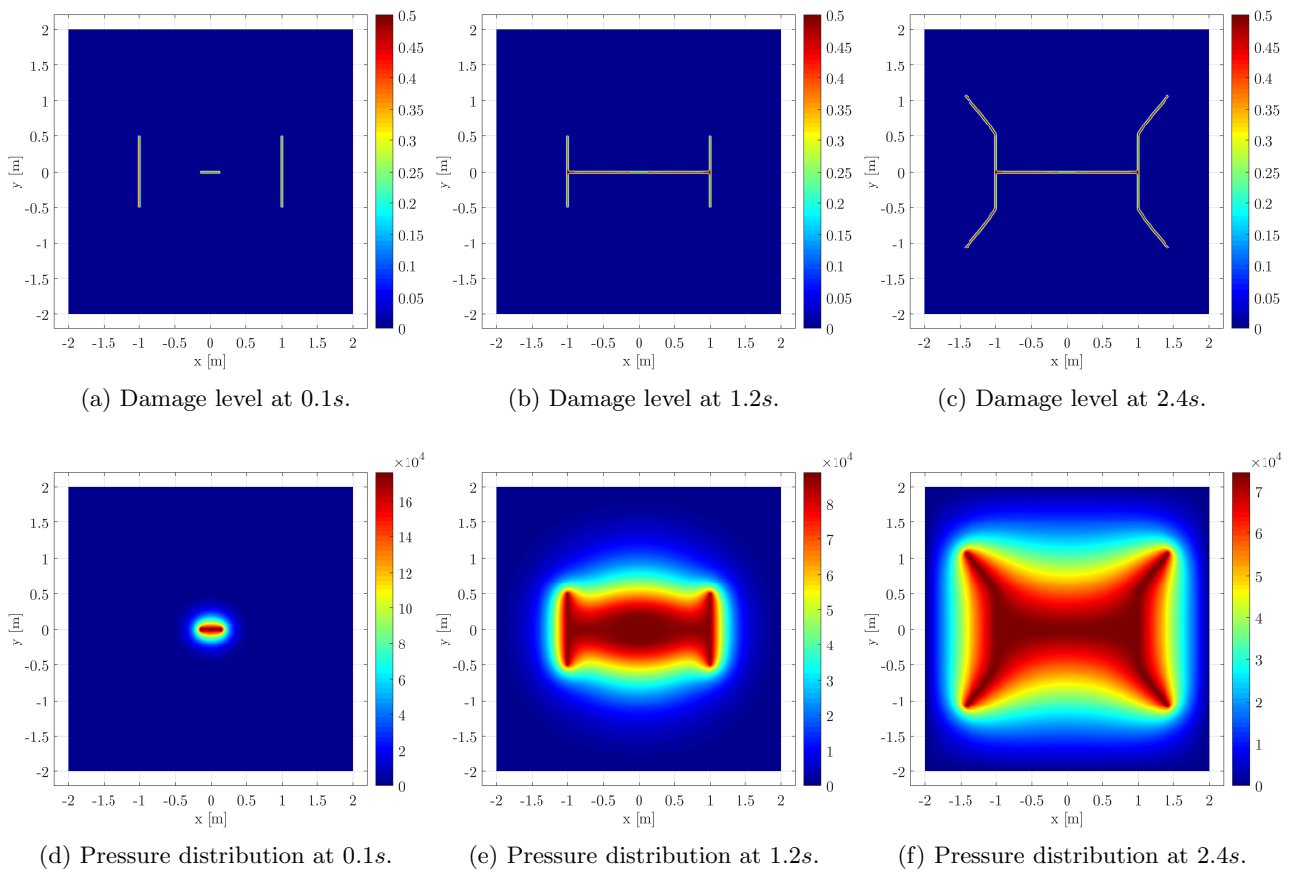


Figure 27: Crack propagation and variation of pressure distribution in case 3 at three time instants.

To investigate the effects of the injection rate on hydraulic fracturing, the geometry in Fig. 23a is adopted with three other different injection rates, which are marked as case 1-1 ($Q = 2 \times 10^{-3} m^3/s$), case 1-2 ($Q = 4 \times 10^{-3} m^3/s$) and case 1-3 ($Q = 6 \times 10^{-3} m^3/s$). Figs. 28a to 28c show the final crack patterns while Figs. 28d to 28f show the corresponding distributions of the pressure. With certain high injection rates, hydraulic crack bifurcation can be observed, which is a typical phenomenon in the dynamic hydraulic fracture. The variation of pressure value at the injection point with time in cases 1, 1-1, 1-2 and 1-3 are plotted in Fig. 29, from which it can be observed that the fracture initiation pressure at the injection point increases with the increase of injection rate and their numerical relationship is plotted in Fig. 30. In addition, as shown in the magnifying frame ② of Fig. 24 and the magnifying frames in Fig. 29, the fluid pressure at the injection point presents a characteristic oscillation, which is consistent with the typical pattern observed experimentally in [115] and the numerical evidence in [29]. In the fracture event the pressure falls rapidly, indicating that the volume of the induced cracks increases faster than the injection rate [116].

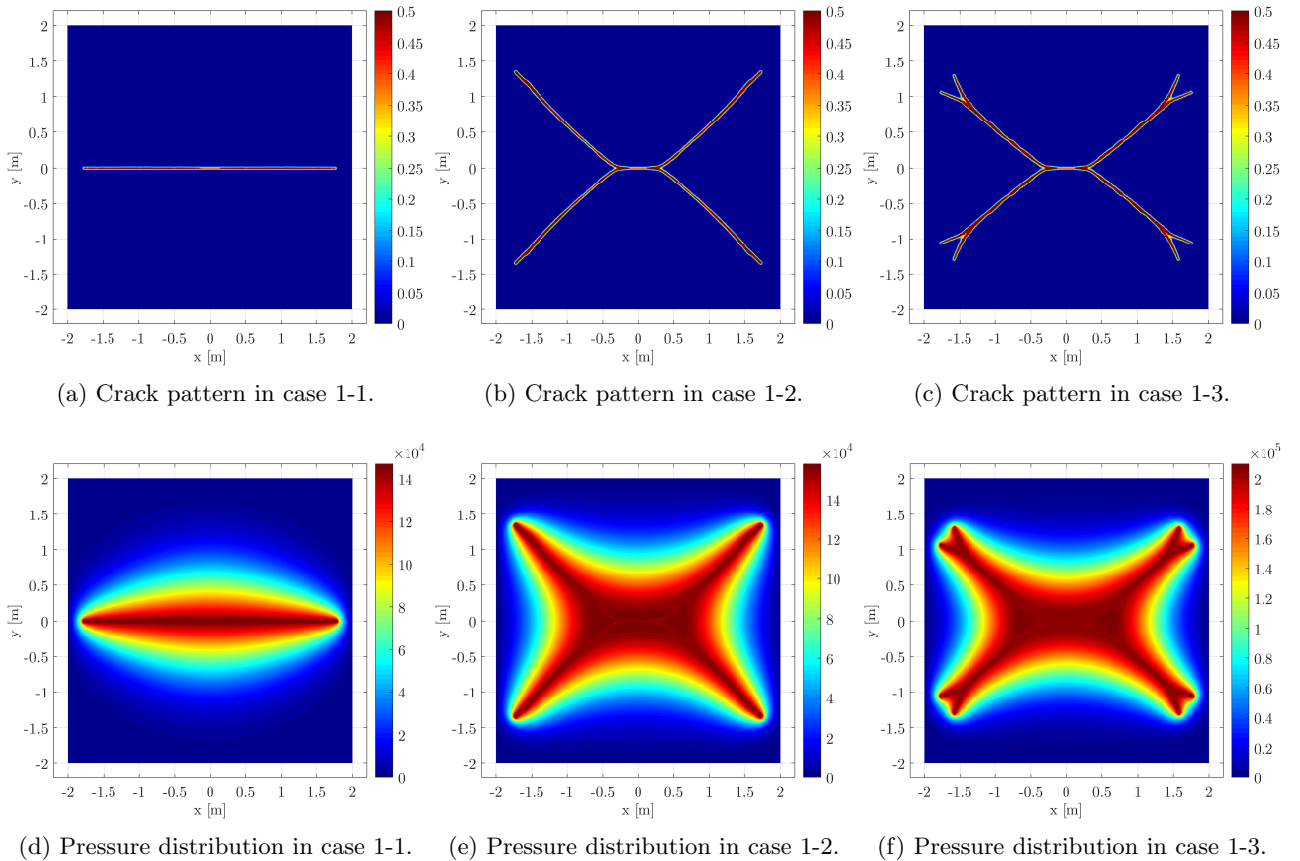


Figure 28: Crack patterns and pressure distributions at the final step of case 1 with different injection rates.

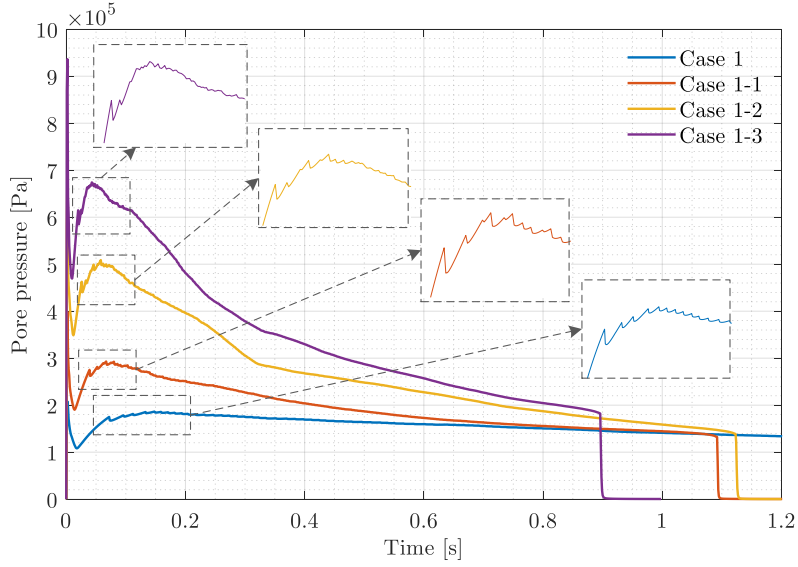


Figure 29: The variation of pressure value at injection point with time of cases 1, 1-1, 1-2 and 1-3.

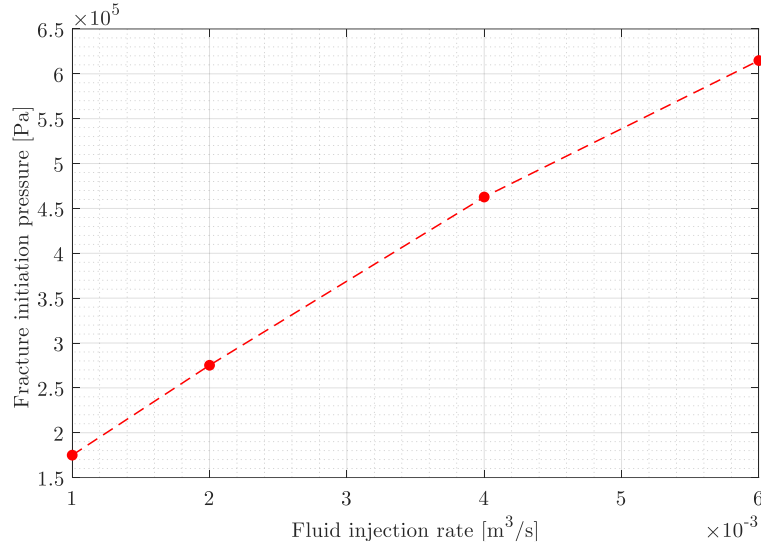


Figure 30: The relationship between the injection rates and the fracture initiation pressures.

5. Conclusions

This paper presents a hybrid FEM and PD modelling approach for simulating hydraulic fracture propagation in saturated porous media. In the proposed approach, FE equations are used to govern the fluid flow, while PD is used to describe the deformation of the solid phase and capture the crack propagation.

Several numerical examples are carried out. First, the proposed approach is validated by two benchmark examples, and the numerical results agree well with the analytical solutions. Then, several numerical examples are presented to further demonstrate the capabilities and the main features of the proposed approach in simulating crack propagation and bifurcation in saturated porous media under pressure- and fluid-driven conditions.

The phenomenon of fluid pressure oscillations is observed in the fluid-driven hydraulic fracture examples, in agreement with experimental observations.

The presented method is one of the first to solve multi-physics problems involving discontinuities by using local models coupled with PD. Similar approaches could be used in the future to effectively simulate crack propagation due to other multi-physics fields: electricity, thermal, chemical, ... the FEM method can be used to solve the multi-physics equations and the coupled Peridynamics model can solve the structural problem in the solid.

List of Symbols

$\boldsymbol{x}, \boldsymbol{x}'$	location vector of material points
\boldsymbol{u}	displacement vector
$\boldsymbol{\xi}$	relative position vector of two material points
$\boldsymbol{\eta}$	relative displacement vector of two material points
$\underline{\boldsymbol{X}}$	reference position vector state
$\underline{\boldsymbol{Y}}$	deformation vector state
\underline{x}	reference position scalar state
\underline{y}	deformation scalar state
$\underline{\boldsymbol{M}}$	unit state in the direction of deformed bond
\underline{e}	extension scalar state
$\underline{\boldsymbol{T}}$	force density vector states
$\ddot{\boldsymbol{u}}$	acceleration vector of material point
\boldsymbol{b}	body force density
\mathcal{H}_x	neighborhood associated with the material point \boldsymbol{x}
θ	volume dilatation value at material point
\underline{e}^d	deviatoric extension state of peridynamic bond
m	weighted volume of material point
\underline{w}	influence function
\underline{t}	force density scalar state
κ, μ	bulk modulus and shear modulus of solid material, respectively
s	stretch value of peridynamic bond
s_c	critical stretch of bonds beyond which bond is broken
G_c	critical energy release rate for mode I fracture
ϱ	characteristic function describing the connection status of bonds
φ_x	damage value at point \boldsymbol{x}
s	local normal deformation (stretch) of bond
s_c	critical stretch of bonds beyond which bond is broken
$\boldsymbol{\sigma}^{tot}, \boldsymbol{\sigma}^{eff}$	total and effective stress tensors
\boldsymbol{I}	unit tensor
p	pore pressure
$\alpha_r, \alpha_T, \alpha_f$	Biot coefficient in reservoir, transition and fracture domains
ρ_r, ρ_T, ρ_f	mass density of media in reservoir, transition and fracture domains

s_r, s_T, s_f	storage coefficient of media in reservoir, transition and fracture domains
n_r, n_T, n_f	porosity of media in reservoir, transition and fracture domains
k_r, k_T, k_f	permeability of media in reservoir, transition and fracture domains
q_r, q_T, q_f	source term in reservoir, transition and fracture domains
K_r, K_w	bulk moduli of solid skeleton and fluid, respectively
ε_v	volumetric strain
μ_w	viscosity coefficient of the fluid
g	gravity acceleration: $9.8m^2/s$
c_1, c_2	threshold values for identifying the three flow domains
χ_r, χ_f	linear indicator functions defined to connect the three flow domains
a	aperture of the crack
$\mathbf{S}, \mathbf{Q}, \mathbf{H}$	compressibility, coupling and permeability matrices of FE equations
$\mathbf{N}_u, \mathbf{N}_p$	shape functions for displacement and pressure, respectively
\mathbf{m}	unit vector replacing \mathbf{I} used in finite element equations
$\mathbf{M}^{PD}, \mathbf{K}^{PD}, \mathbf{Q}^{PD}$	mass, stiffness and coupling matrices of PD equations
E	Young's modulus of solids
ν	Poisson's ratio of solids

Acknowledgements

This work has been jointly supported by the National Key Research and Development Program of China (2017YFC1501102), the National Natural Science Foundation of China (Grant Nos. 51679068 and 11872172), the Fundamental Research Funds for Central Universities (2017B704X14), the Post-graduate Research & Practice Innovation Program of Jiangsu Province (Grant No. KYCX17_0479), and the China Scholarship Council (No. 201706710018).

U. Galvanetto and M. Zaccariotto acknowledge the support they received from MIUR under the research project PRIN2017-DEVISU and from University of Padua under the research projects BIRD2018 NR.183703/18 and BIRD2017 NR.175705/17.

F. Pesavento would like to acknowledge the project 734370-BESTOFRAC “Environmentally best practices and optimisation in hydraulic fracturing for shale gas/oil development”-H2020-MSCA-RISE-2016 and the support he received from University of Padua under the research project BIRD197110/19 “Innovative models for the simulation of fracturing phenomena in structural engineering and geomechanics”.

B.A. Schrefler gratefully acknowledges the support of the Technische Universität München - Institute for Advanced Study, funded by the German Excellence Initiative and the TUV SÜD Foundation.

The authors thank also C. Peruzzo for useful discussions.

References

- [1] S. Zhou, X. Zhuang, T. Rabczuk, Phase-field modeling of fluid-driven dynamic cracking in porous media, *Computer Methods in Applied Mechanics and Engineering* (2019).
- [2] S. Zhou, X. Zhuang, T. Rabczuk, A phase-field modeling approach of fracture propagation in poroelastic media, *Engineering Geology* 240 (2018) 189–203.
- [3] R. D. Vidic, S. L. Brantley, J. M. Vandenbossche, D. Yoxtheimer, J. D. Abad, Impact of shale gas development on regional water quality, *science* 340 (6134) (2013) 1235009.
- [4] F. Ren, G. Ma, L. Fan, Y. Wang, H. Zhu, Equivalent discrete fracture networks for modelling fluid flow in highly fractured rock mass, *Engineering geology* 229 (2017) 21–30.
- [5] A. Mikelic, M. F. Wheeler, T. Wick, A phase field approach to the fluid filled fracture surrounded by a poroelastic medium, ICES report 1315 (2013).
- [6] D. Z. Turner, A non-local model for fluid-structure interaction with applications in hydraulic fracturing, *International Journal for Computational Methods in Engineering Science and Mechanics* 14 (5) (2013) 391–400.
- [7] H. Ouchi, A. Katiyar, J. York, J. T. Foster, M. M. Sharma, A fully coupled porous flow and geomechanics model for fluid driven cracks: a peridynamics approach, *Computational Mechanics* 55 (3) (2015) 561–576.
- [8] H. Ouchi, J. T. Foster, M. M. Sharma, Effect of reservoir heterogeneity on the vertical migration of hydraulic fractures, *Journal of Petroleum Science and Engineering* 151 (2017) 384–408.
- [9] S. Lee, M. F. Wheeler, T. Wick, Pressure and fluid-driven fracture propagation in porous media using an adaptive finite element phase field model, *Computer Methods in Applied Mechanics and Engineering* 305 (2016) 111–132.
- [10] B. Lecampion, A. Bungler, X. Zhang, Numerical methods for hydraulic fracture propagation: a review of recent trends, *Journal of natural gas science and engineering* 49 (2018) 66–83.
- [11] L. Simoni, S. Secchi, Cohesive fracture mechanics for a multi-phase porous medium, *Engineering Computations* 20 (5/6) (2003) 675–698.
- [12] B. A. Schrefler, S. Secchi, L. Simoni, On adaptive refinement techniques in multi-field problems including cohesive fracture, *Computer methods in applied mechanics and engineering* 195 (4-6) (2006) 444–461.
- [13] S. Secchi, L. Simoni, B. A. Schrefler, Mesh adaptation and transfer schemes for discrete fracture propagation in porous materials, *International journal for numerical and analytical methods in geomechanics* 31 (2) (2007) 331–345.
- [14] Z. Chen, A. Bungler, X. Zhang, R. G. Jeffrey, Cohesive zone finite element-based modeling of hydraulic fractures, *Acta Mechanica Solida Sinica* 22 (5) (2009) 443–452.
- [15] E. Sarris, P. Papanastasiou, Modeling of hydraulic fracturing in a poroelastic cohesive formation, *International Journal of Geomechanics* 12 (2) (2011) 160–167.
- [16] B. Carrier, S. Granet, Numerical modeling of hydraulic fracture problem in permeable medium using cohesive zone model, *Engineering fracture mechanics* 79 (2012) 312–328.
- [17] E. Sarris, P. Papanastasiou, Numerical modeling of fluid-driven fractures in cohesive poroelastoplastic continuum, *International Journal for Numerical and Analytical Methods in Geomechanics* 37 (12) (2013) 1822–1846.
- [18] Y. Yao, L. Liu, L. M. Keer, Pore pressure cohesive zone modeling of hydraulic fracture in quasi-brittle rocks, *Mechanics of Materials* 83 (2015) 17–29.
- [19] A. Needleman, Some issues in cohesive surface modeling, *Procedia IUTAM* 10 (2014) 221–246.
- [20] T. Belytschko, R. Gracie, G. Ventura, A review of extended/generalized finite element methods for material modeling, *Modelling and Simulation in Materials Science and Engineering* 17 (4) (2009) 043001.
- [21] J. Réthoré, R. d. Borst, M.-A. Abellan, A two-scale approach for fluid flow in fractured porous media, *International*

Journal for Numerical Methods in Engineering 71 (7) (2007) 780–800.

- [22] B. Lecampion, An extended finite element method for hydraulic fracture problems, *Communications in Numerical Methods in Engineering* 25 (2) (2009) 121–133.
- [23] E. Gordeliy, A. Peirce, Coupling schemes for modeling hydraulic fracture propagation using the xfem, *Computer Methods in Applied Mechanics and Engineering* 253 (2013) 305–322.
- [24] M. Vahab, S. Akhondzadeh, A. Khoei, N. Khalili, An x-fem investigation of hydro-fracture evolution in naturally-layered domains, *Engineering Fracture Mechanics* 191 (2018) 187–204.
- [25] M. Faivre, B. Paul, F. Golfier, R. Giot, P. Massin, D. Colombo, 2d coupled hm-xfem modeling with cohesive zone model and applications to fluid-driven fracture network, *Engineering Fracture Mechanics* 159 (2016) 115–143.
- [26] T. Mohammadnejad, A. Khoei, An extended finite element method for hydraulic fracture propagation in deformable porous media with the cohesive crack model, *Finite Elements in Analysis and Design* 73 (2013) 77–95.
- [27] H. Wang, Numerical modeling of non-planar hydraulic fracture propagation in brittle and ductile rocks using xfem with cohesive zone method, *Journal of Petroleum Science and Engineering* 135 (2015) 127–140.
- [28] B. Paul, M. Faivre, P. Massin, R. Giot, D. Colombo, F. Golfier, A. Martin, 3d coupled hm-xfem modeling with cohesive zone model and applications to non planar hydraulic fracture propagation and multiple hydraulic fractures interference, *Computer Methods in Applied Mechanics and Engineering* 342 (2018) 321–353.
- [29] T. D. Cao, F. Hussain, B. A. Schrefler, Porous media fracturing dynamics: stepwise crack advancement and fluid pressure oscillations, *Journal of the Mechanics and Physics of Solids* 111 (2018) 113–133.
- [30] B. L. Karihaloo, Q. Xiao, Modelling of stationary and growing cracks in fe framework without remeshing: a state-of-the-art review, *Computers & Structures* 81 (3) (2003) 119–129.
- [31] P. Gupta, C. A. Duarte, Simulation of non-planar three-dimensional hydraulic fracture propagation, *International Journal for Numerical and Analytical Methods in Geomechanics* 38 (13) (2014) 1397–1430.
- [32] M. Ambati, T. Gerasimov, L. De Lorenzis, A review on phase-field models of brittle fracture and a new fast hybrid formulation, *Computational Mechanics* 55 (2) (2015) 383–405.
- [33] C. Miehe, F. Welschinger, M. Hofacker, Thermodynamically consistent phase-field models of fracture: Variational principles and multi-field fe implementations, *International Journal for Numerical Methods in Engineering* 83 (10) (2010) 1273–1311.
- [34] C. Miehe, S. Mauthe, S. Teichtmeister, Minimization principles for the coupled problem of darcy–biot-type fluid transport in porous media linked to phase field modeling of fracture, *Journal of the Mechanics and Physics of Solids* 82 (2015) 186–217.
- [35] A. Mikelic, M. F. Wheeler, T. Wick, A phase-field method for propagating fluid-filled fractures coupled to a surrounding porous medium, *Multiscale Modeling & Simulation* 13 (1) (2015) 367–398.
- [36] Z. A. Wilson, C. M. Landis, Phase-field modeling of hydraulic fracture, *Journal of the Mechanics and Physics of Solids* 96 (2016) 264–290.
- [37] E. Siebrits, A. P. Peirce, An efficient multi-layer planar 3d fracture growth algorithm using a fixed mesh approach, *International journal for numerical methods in engineering* 53 (3) (2002) 691–717.
- [38] K. Yamamoto, T. Shimamoto, S. Sukemura, Multiple fracture propagation model for a three-dimensional hydraulic fracturing simulator, *International Journal of geomechanics* 4 (1) (2004) 46–57.
- [39] E. Gordeliy, E. Detournay, A fixed grid algorithm for simulating the propagation of a shallow hydraulic fracture with a fluid lag, *International Journal for numerical and analytical methods in geomechanics* 35 (5) (2011) 602–629.
- [40] J. Rungamornrat, M. F. Wheeler, M. E. Mear, A numerical technique for simulating nonplanar evolution of hydraulic fractures, in: *SPE Annual Technical Conference and Exhibition, ATCE 2005*, 2005.

- [41] G. Xu, S.-W. Wong, Interaction of multiple non-planar hydraulic fractures in horizontal wells, in: IPTC 2013: International Petroleum Technology Conference, 2013.
- [42] S. Samimi, A. Pak, A fully coupled element-free galerkin model for hydro-mechanical analysis of advancement of fluid-driven fractures in porous media, *International Journal for Numerical and Analytical Methods in Geomechanics* 40 (16) (2016) 2178–2206.
- [43] T. Douillet-Grellier, R. Pramanik, K. Pan, A. Albaiz, B. D. Jones, H. Pourpak, J. R. Williams, et al., Mesh-free numerical simulation of pressure-driven fractures in brittle rocks, in: SPE Hydraulic Fracturing Technology Conference, Society of Petroleum Engineers, 2016.
- [44] B. Damjanac, C. Detournay, P. A. Cundall, Application of particle and lattice codes to simulation of hydraulic fracturing, *Computational Particle Mechanics* 3 (2) (2016) 249–261.
- [45] B. Damjanac, C. Detournay, et al., Three-dimensional numerical model of hydraulic fracturing in fractured rock masses, in: ISRM International Conference for Effective and Sustainable Hydraulic Fracturing, International Society for Rock Mechanics and Rock Engineering, 2013.
- [46] P. Grassl, C. Fahy, D. Gallipoli, S. J. Wheeler, On a 2d hydro-mechanical lattice approach for modelling hydraulic fracture, *Journal of the Mechanics and Physics of Solids* 75 (2015) 104–118.
- [47] Q. Zhao, A. Lisjak, O. Mahabadi, Q. Liu, G. Grasselli, Numerical simulation of hydraulic fracturing and associated microseismicity using finite-discrete element method, *Journal of Rock Mechanics and Geotechnical Engineering* 6 (6) (2014) 574–581.
- [48] C. Yan, H. Zheng, G. Sun, X. Ge, Combined finite-discrete element method for simulation of hydraulic fracturing, *Rock Mechanics and Rock Engineering* 49 (4) (2016) 1389–1410.
- [49] J. Jiang, R. M. Younis, et al., Hybrid coupled discrete-fracture/matrix and multicontinuum models for unconventional-reservoir simulation, *SPE Journal* 21 (03) (2016) 1–009.
- [50] F. Zhang, E. Dontsov, M. Mack, Fully coupled simulation of a hydraulic fracture interacting with natural fractures with a hybrid discrete-continuum method, *International Journal for Numerical and Analytical Methods in Geomechanics* 41 (13) (2017) 1430–1452.
- [51] Y. Yang, X. Tang, H. Zheng, Q. Liu, Z. Liu, Hydraulic fracturing modeling using the enriched numerical manifold method, *Applied Mathematical Modelling* 53 (2018) 462–486.
- [52] Z. Wu, L. N. Y. Wong, Extension of numerical manifold method for coupled fluid flow and fracturing problems, *International Journal for Numerical and Analytical Methods in Geomechanics* 38 (18) (2014) 1990–2008.
- [53] S. Peng, Z. Zhang, J. Mou, B. Zhao, Z. Liu, A. Ghassemi, Hydraulic fracture simulation with hydro-mechanical coupled discretized virtual internal bond, *Journal of Petroleum Science and Engineering* 169 (2018) 504–517.
- [54] E. Milanese, O. Yılmaz, J.-F. Molinari, B. Schrefler, Avalanches in dry and saturated disordered media at fracture, *Physical Review E* 93 (4) (2016) 043002.
- [55] T. D. Cao, E. Milanese, E. W. Remij, P. Rizzato, J. J. Remmers, L. Simoni, J. M. Huyghe, F. Hussain, B. A. Schrefler, Interaction between crack tip advancement and fluid flow in fracturing saturated porous media, *Mechanics Research Communications* 80 (2017) 24–37.
- [56] S. A. Silling, Reformulation of elasticity theory for discontinuities and long-range forces, *Journal of the Mechanics and Physics of Solids* 48 (1) (2000) 175–209.
- [57] S. A. Silling, E. Askari, A meshfree method based on the peridynamic model of solid mechanics, *Computers & structures* 83 (17-18) (2005) 1526–1535.
- [58] U. Galvanetto, T. Mudric, A. Shojaei, M. Zaccariotto, An effective way to couple fem meshes and peridynamics grids for the solution of static equilibrium problems, *Mechanics Research Communications* 76 (2016) 41–47.

- [59] T. Ni, M. Zaccariotto, Q.-Z. Zhu, U. Galvanetto, Static solution of crack propagation problems in peridynamics, *Computer Methods in Applied Mechanics and Engineering* 346 (2019) 126–151.
- [60] Y. Wang, X. Zhou, M. Kou, An improved coupled thermo-mechanic bond-based peridynamic model for cracking behaviors in brittle solids subjected to thermal shocks, *European Journal of Mechanics-A/Solids* 73 (2019) 282–305.
- [61] Y. Wang, X. Zhou, T. Zhang, Size effect of thermal shock crack patterns in ceramics: Insights from a nonlocal numerical approach, *Mechanics of Materials* 137 (2019) 103133.
- [62] S. A. Silling, M. Epton, O. Weckner, J. Xu, E. Askari, Peridynamic states and constitutive modeling, *Journal of Elasticity* 88 (2) (2007) 151–184.
- [63] Q.-z. Zhu, T. Ni, Peridynamic formulations enriched with bond rotation effects, *International Journal of Engineering Science* 121 (2017) 118–129.
- [64] Y. Wang, X. Zhou, Y. Wang, Y. Shou, A 3-d conjugated bond-pair-based peridynamic formulation for initiation and propagation of cracks in brittle solids, *International Journal of Solids and Structures* 134 (2018) 89–115.
- [65] S. R. Chowdhury, M. M. Rahaman, D. Roy, N. Sundaram, A micropolar peridynamic theory in linear elasticity, *International Journal of Solids and Structures* 59 (2015) 171–182.
- [66] Y. Zhang, P. Qiao, An axisymmetric ordinary state-based peridynamic model for linear elastic solids, *Computer Methods in Applied Mechanics and Engineering* 341 (2018) 517–550.
- [67] T. Zhang, X. Zhou, A modified axisymmetric ordinary state-based peridynamics with shear deformation for elastic and fracture problems in brittle solids, *European Journal of Mechanics-A/Solids* (2019) 103810.
- [68] V. Diana, S. Casolo, A bond-based micropolar peridynamic model with shear deformability: Elasticity, failure properties and initial yield domains, *International Journal of Solids and Structures* 160 (2019) 201–231.
- [69] A. Katiyar, J. T. Foster, H. Ouchi, M. M. Sharma, A peridynamic formulation of pressure driven convective fluid transport in porous media, *Journal of Computational Physics* 261 (2014) 209–229.
- [70] R. Jabakhanji, R. H. Mohtar, A peridynamic model of flow in porous media, *Advances in water resources* 78 (2015) 22–35.
- [71] H. Ouchi, A. Katiyar, J. T. Foster, M. M. Sharma, et al., A peridynamics model for the propagation of hydraulic fractures in naturally fractured reservoirs, *SPE Journal* 22 (04) (2017) 1–082.
- [72] S. Nadimi, I. Miscovic, J. McLennan, A 3d peridynamic simulation of hydraulic fracture process in a heterogeneous medium, *Journal of Petroleum Science and Engineering* 145 (2016) 444–452.
- [73] S. Oterkus, E. Madenci, E. Oterkus, Fully coupled poroelastic peridynamic formulation for fluid-filled fractures, *Engineering geology* 225 (2017) 19–28.
- [74] H. Zhang, H. Li, H. Ye, Y. Zheng, A coupling peridynamic approach for the consolidation and dynamic analysis of saturated porous media, *Computational Mechanics* (2019) 1–17.
- [75] D. Turner, A coupled local-nonlocal framework for modeling hydraulic fracturing in the karoo, in: *Research and Applications in Structural Engineering, Mechanics and Computation*, CRC Press, 2013, pp. 235–236.
- [76] M. Zaccariotto, T. Mudric, D. Tomasi, A. Shojaei, U. Galvanetto, Coupling of fem meshes with peridynamic grids, *Computer Methods in Applied Mechanics and Engineering* 330 (2018) 471–497.
- [77] O. C. Zienkiewicz, R. L. Taylor, P. Nithiarasu, J. Zhu, *The finite element method*, Vol. 3, McGraw-hill London, 1977.
- [78] I. M. Smith, D. V. Griffiths, L. Margetts, *Programming the finite element method*, John Wiley & Sons, 2013.
- [79] P. Underwood, Dynamic relaxation, *Computational Methods for Transient Analysis* 1 (1983) 245–265.
- [80] B. Kilic, E. Madenci, An adaptive dynamic relaxation method for quasi-static simulations using the peridynamic theory, *Theoretical and Applied Fracture Mechanics* 53 (3) (2010) 194–204.

- [81] T. Ni, M. Zaccariotto, Q.-Z. Zhu, U. Galvanetto, Coupling of fem and ordinary state-based peridynamics for brittle failure analysis in 3d, *Mechanics of Advanced Materials and Structures*, (2019). doi:10.1080/15376494.2019.1602237.
- [82] Q. Le, W. Chan, J. Schwartz, A two-dimensional ordinary, state-based peridynamic model for linearly elastic solids, *International Journal for Numerical Methods in Engineering* 98 (8) (2014) 547–561.
- [83] G. Sarego, Q. V. Le, F. Bobaru, M. Zaccariotto, U. Galvanetto, Linearized state-based peridynamics for 2-d problems, *International Journal for Numerical Methods in Engineering* 108 (10) (2016) 1174–1197.
- [84] F. Bobaru, J. T. Foster, P. H. Geubelle, S. A. Silling, *Handbook of peridynamic modeling*, CRC press, 2016.
- [85] Q. Van Le, F. Bobaru, Objectivity of state-based peridynamic models for elasticity, *Journal of Elasticity* 131 (1) (2018) 1–17.
- [86] Y. Zhang, P. Qiao, A new bond failure criterion for ordinary state-based peridynamic mode ii fracture analysis, *International Journal of Fracture* 215 (1-2) (2019) 105–128.
- [87] J. T. Foster, S. A. Silling, W. Chen, An energy based failure criterion for use with peridynamic states, *International Journal for Multiscale Computational Engineering* 9 (6) (2011).
- [88] H. Zhang, P. Qiao, A state-based peridynamic model for quantitative fracture analysis, *International Journal of Fracture* 211 (1-2) (2018) 217–235.
- [89] H. Zhang, P. Qiao, A state-based peridynamic model for quantitative elastic and fracture analysis of orthotropic materials, *Engineering Fracture Mechanics* 206 (2019) 147–171.
- [90] T. L. Warren, S. A. Silling, A. Askari, O. Weckner, M. A. Epton, J. Xu, A non-ordinary state-based peridynamic method to model solid material deformation and fracture, *International Journal of Solids and Structures* 46 (5) (2009) 1186–1195.
- [91] D. Dipasquale, G. Sarego, M. Zaccariotto, U. Galvanetto, A discussion on failure criteria for ordinary state-based peridynamics, *Engineering Fracture Mechanics* 186 (2017) 378–398.
- [92] D. J. Littlewood, Roadmap for peridynamic software implementation, SAND Report, Sandia National Laboratories, Albuquerque, NM and Livermore, CA (2015).
- [93] T. Ni, Q.-z. Zhu, L.-Y. Zhao, P.-F. Li, Peridynamic simulation of fracture in quasi brittle solids using irregular finite element mesh, *Engineering Fracture Mechanics* 188 (2018) 320–343.
- [94] K. Zhang, T. Ni, G. Sarego, M. Zaccariotto, Q. Zhu, U. Galvanetto, Experimental and numerical fracture analysis of the plain and polyvinyl alcohol fiber-reinforced ultra-high-performance concrete structures, *Theoretical and Applied Fracture Mechanics* 108 (2020) 102566.
- [95] R. W. Lewis, B. A. Schrefler, *The finite element method in the static and dynamic deformation and consolidation of porous media*, John Wiley, 1998.
- [96] O. C. Zienkiewicz, A. Chan, M. Pastor, B. Schrefler, T. Shiomi, *Computational Geomechanics: With Special Reference to Earthquake Engineering*, John Wiley & Sons, 1999.
- [97] J. R. York, et al., Advanced hydraulic fracture modeling: peridynamics, inelasticity, and coupling to fem, Ph.D. thesis (2018).
- [98] C. J. Van Duijn, A. Mikelić, T. Wick, A monolithic phase-field model of a fluid-driven fracture in a nonlinear poroelastic medium, *Mathematics and Mechanics of Solids* 24 (5) (2019) 1530–1555.
- [99] R. Zimmerman, G. Bodvarsson, Hydraulic conductivity of rock fractures, Tech. rep., Lawrence Berkeley Lab. (1994).
- [100] C. Peruzzo, D. Cao, E. Milanese, P. Favia, F. Pesavento, F. Hussain, B. Schrefler, Dynamics of fracturing saturated porous media and self-organization of rupture, *European Journal of Mechanics-A/Solids* 74 (2019) 471–484.

- [101] O. C. Zienkiewicz, R. L. Taylor, R. L. Taylor, *The finite element method: solid mechanics*, Vol. 2, Butterworth-Heinemann, 2000.
- [102] W. Frei, Solving multiphysics problems, <https://www.comsol.com/blogs/solving-multiphysics-problems/>, accessed December 16, 2013.
- [103] H. F. Wang, *Theory of linear poroelasticity with applications to geomechanics and hydrogeology*, Princeton University Press, 2017.
- [104] I. Sneddon, M. Lowengrub, *Crack problems in the classical theory of elasticity*, John Wiley & Sons, New York (1969) 29.
- [105] A. M. Linkov, Universal asymptotic umbrella for hydraulic fracture modeling, arXiv preprint arXiv:1404.4165 (2014).
- [106] A. P. Bunger, E. Detournay, D. I. Garagash, Toughness-dominated hydraulic fracture with leak-off, *International journal of fracture* 134 (2) (2005) 175–190.
- [107] H. J. De Pater, et al., Hydraulic fracture containment: New insights into mapped geometry., in: *SPE Hydraulic Fracturing Technology Conference*, Society of Petroleum Engineers, 2015.
- [108] T. J. Boone, A. R. Ingraffea, A numerical procedure for simulation of hydraulically-driven fracture propagation in poroelastic media, *International Journal for Numerical and Analytical Methods in Geomechanics* 14 (1) (1990) 27–47.
- [109] D. Spence, P. Sharp, Self-similar solutions for elastohydrodynamic cavity flow, *Proceedings of the Royal Society of London. A. Mathematical and Physical Sciences* 400 (1819) (1985) 289–313.
- [110] A. Baykin, S. Golovin, Application of the fully coupled planar 3d poroelastic hydraulic fracturing model to the analysis of the permeability contrast impact on fracture propagation, *Rock Mechanics and Rock Engineering* 51 (10) (2018) 3205–3217.
- [111] M. Parchei Esfahani, R. Gracie, On the undrained and drained hydraulic fracture splits, *International Journal for Numerical Methods in Engineering* 118 (12) (2019) 741–763.
- [112] J. Geertsma, F. De Klerk, et al., A rapid method of predicting width and extent of hydraulically induced fractures, *Journal of petroleum technology* 21 (12) (1969) 1–571.
- [113] M. Chen, S. Zhang, S. Li, X. Ma, X. Zhang, Y. Zou, An explicit algorithm for modeling planar 3d hydraulic fracture growth based on a super-time-stepping method, *International Journal of Solids and Structures* (2020).
- [114] H. Huang, E. Detournay, Discrete element modeling of tool-rock interaction ii: rock indentation, *International Journal for Numerical and Analytical Methods in Geomechanics* 37 (13) (2013) 1930–1947.
- [115] T. Lhomme, C. De Pater, P. Helfferich, et al., Experimental study of hydraulic fracture initiation in colton sandstone, in: *SPE/ISRM Rock Mechanics Conference*, Society of Petroleum Engineers, 2002.
- [116] D. Okland, G. K. Gabrielsen, J. Gjerde, S. Koen, E. L. Williams, et al., The importance of extended leak-off test data for combatting lost circulation, in: *SPE/ISRM Rock Mechanics Conference*, Society of Petroleum Engineers, 2002.